Postprint for: Dastjerdi, S, Malikan, M, Eremeyev, VA, Akgöz, B, Civalek, Ö., Mechanical simulation of artificial gravity in torus-shaped and cylindrical spacecraft. ACTA ASTRONAUTICA, vol. 179 (2020), pp. 330-344, DOI: 10.1016/j.actaastro.2020.11.005

Mechanical simulation of artificial gravity in torus-shaped and cylindrical spacecraft

Shahriar Dastjerdi [a], Mohammad Malikan[b], Victor A. Eremeyev [b, c*], Bekir Akgöz [a], Ömer Civalek [d]

[a] Division of Mechanics, Civil Engineering Department, Akdeniz University, Antalya, Turkey

[b] Department of Mechanics of Materials and Structures, Faculty of Civil and Environmental Engineering, Gdansk University of Technology, Gdansk, Poland

[c] Research Institute for Mechanics, Nizhny Novgorod Lobachevsky State University, Russia

[d] China Medical University, Taichung, Taiwan

* Corresponding author:

victor.eremeev@pg.edu.pl, eremeyev.victor@gmail.com

ABSTRACT

Large deformations and stress analyses in two types of space structures that are intended for people to live in space have been studied in this research. The structure under analysis is assumed to rotate around the central axis to create artificial gravitational acceleration equal to the gravity on the Earth's surface. The analysis is fully dynamic, which is formulated based on the energy method by using the first-order shear deformation shell theory in two systems, cylindrical and torus. Also, the nonlinear von Kármán strain field has been assumed. The obtained set of partial differential equations has been solved using the semi-analytical polynomial solution method (SAPM). The main purpose of this paper is to study the effects of unusual conditions in the space outside the Earth's atmosphere (which is a complete vacuum

environment without pressure) on the strength of the analyzed structure. The numerical results of the governing equations have been evaluated using those of other studies and the simulation efficiency performed in this research has been proven. Finally, the effect of important parameters on the numerical results, including the angular velocity of the structure (which causes artificial gravity), the amount of imposed mechanical and hygro-thermal loads, the structure size and material specifications have been investigated in more detail.

Keywords: Torus-shaped and cylindrical space structures, Artificial gravity, First-order shear deformation theory (FSDT), Functionally graded materials

1. Introduction

A spacecraft is a vehicle or device designed to fly in space and is used in a variety of fields, including communications, ground surveillance, meteorology, navigation, planetary exploration, and human and cargo transportation. Not all space crafts, except single-stage models, can reach space alone and require a launch vehicle or carrier rocket to do so. Several important attached bodies compose a spacecraft including communication antennas, solar arrays, and living chambers, etc. The focal point in designing space crafts can be their lightweight structures, stability, equilibrium in dynamic movements and structures including hot and cold parts. To manage these vital conditions in the design particularly manufacturing, novel experimental techniques emerged leading to high-quality parts. The passive mechanical loads, internal pressures, effects of meteoroids, inner humidity, variations of temperature, oscillations, passive and active noises, etc. can be witnessed in a spacecraft during working [1-4].

The harmful effects of prolonged weightlessness in spaceflight for astronauts have been expressed as a serious discussion. These detrimental impacts can be, for example, weakening of muscles and reduction in bone density of people. One of the tackling ways for this problem

can be the creation of artificial gravity that is sometimes named as pseudo-gravity. This can happen by exerting rotational movement and creating inertia forces. This means, in a frame due to its rotation, a produced centrifugal force can provide artificial gravity [5]. To envisage such a frame, a torus and or a cylindrical shape have been contemplating by aerospace engineers for decades.

In a spacecraft cabin, when astronauts breathe, it can generate moisture. The sweating or breathing of an astronaut establishes moisture. In fact, perspiration and respiration shifts to the spacecraft parts and finally may destruct them. Thus, the humidity influence is noteworthy to be predicted while designing the space crafts. Accordingly, the astronauts, equipment, and spacecraft remain safe. This way, by means of forecasting the hygral impacts on a spacecraft, it can aid us to keep everything secure. It can lead to problems for both astronauts and spacecraft structure if the humidity value increases. In a point of fact, internal pressure can be appeared in the spacecraft resulted from the hygral percentage. Physically, when the air condenses, there would be a mechanical pressure [6]. So, as the influence of the moisture on the spacecraft would be crucial, this paper will address this effect as well.

In terms of the mechanism function of space, space would be entirely unpredictable in comparison with the Earth due to several situations that affect it. There is a complete vacuum, weightlessness, extremely variable temperature, and all kinds of radiation. Sun radiation can heat up the spacecraft components confronted with the sun. Also, the same parts can withstand cold below zero when moving in the shadow part of the Earth. Consequently, the spacecraft is exposed to the thermal changes due to the solar flux and spacecraft itself [7-8]. Thus, the thermal environment of the space can harm the flexible structures of the spacecraft and it can be stated that the spacecraft is susceptible to be seriously damaged by sunlight and thermal radiation during a maneuver in orbit [9]. Moreover, as this temperature variation is a time-dependent one,

it would induce oscillations into the section of the solar arrays originated from periodic sunlight [10-17]. So, temperature-time dependent coupling dynamic analysis is an earnestly request addressed in this paper.

Knowledge of the dynamics of the basic structures of the spacecraft seriously requires further studies. This led us to prepare this research study. We model the cylinder and torus parts of the spacecraft based on the computational dynamic and theoretical investigations. To assign material for the parts, we develop the functionally graded (FG) properties for the material. The first-order shear deformation theory sets out the theoretical time-dependent relations. We assume an artificial gravity into mathematical modeling and assess its effect on the problem in detail. We investigated abnormal situations of the space on the dimensions of spacecraft structures. In other words, under what conditions can one be completely sure of its design in terms of material and geometric dimensions. Because the necessary measures to save the lives of people living in the space, which is a vital issue, must be considered. As mentioned before, temperature variations and overload hygral cause serious effects on the parts of the spacecraft. Hence, such effects are implemented in theoretical dynamic modeling. We present and indicate the theoretical modeling based on general media in order to be able to have various strain fields originated from the media. Numerical outcomes are obtained by means of SAPM technique which is a semi-analytical solution [18-20]. Graphical results are demonstrated for the two mentioned chamber geometries, namely cylindrical and torus on the basis of the stress evaluation. We intend to display the numerical results in an optimized way. In doing so, the admissible tolerances beside critical factors are defined and determined. It is guessed that the chamber parts of the spacecraft can be affected remarkably by the internal pressure. This point brings us to measure the internal pressure on the cylindrical and torus living sections. In addition to these, another eminent factor would be the rotational speed in the dynamics of the spacecraft. The rotational velocity is estimated for both geometries with the difference that the cylinder has

one and the torus structure has two independent axes. Ultimately, we reveal numerically impacts of essential factors established pictorially. This research can provide very interesting scientific perspectives for researchers who examine the artificial gravity analysis of torus and cylindrical shaped space station structures.

In mentioning the highlights of the present research, one can state that for the first time on the basis of a mathematical modelling, we analyze the residence structures of a spacecraft. Moreover, we simulate the effects of artificial gravity in the residence structures. On the other side, we also consider the temperature variation on the space structures and its impact on the created stresses in the structures. These are the most significant achieved items of the present study.

2. Artificial gravity

The lives of astronauts in weightless conditions have far-reaching consequences for their health, especially if they are considered long-term. Muscles gradually weaken and even heart problems, vascular diseases, muscle shrinkage, and dysfunction of internal organs will be inevitable. To solve these problems, astronauts usually exercise regularly at the space station so as not to be exposed to the adverse effects of weightlessness, and these risks are minimized. Another way is to create artificial gravity conditions. According to Einstein's theory of general relativity, the gravity field is nothing but relative acceleration. For example, if a satellite (Fig. 1) orbits the Earth, Newton's second law can be written according to the equation $m(R_E + D)\omega^2 = mg \rightarrow \omega = \sqrt{\frac{g}{(R_E+D)}}, V_{Lin} = \sqrt{(R_E + D)g}$ so that the satellite orbits the Earth at that particular altitude (R_E,D and g are the radius of Earth, distance of rotating object from the Earth's surface and the gravitational acceleration on the Earth's surface at equator equals to $g = 9.806\frac{m}{s^2}$)

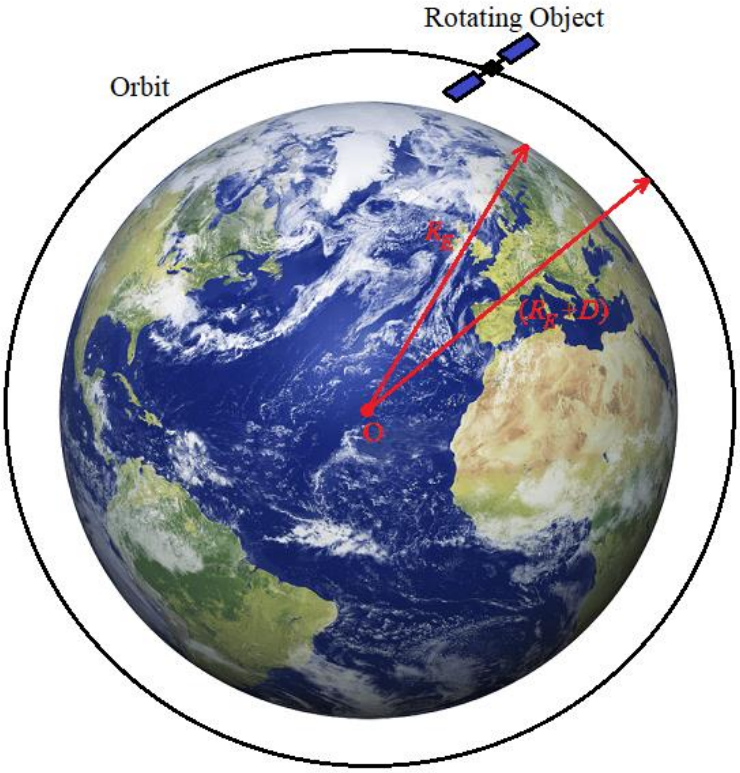

Fig. 1. Rotating object in an orbit around the Earth

Parameters ω $(\frac{Rad}{s})$ and V_{Lin} $(\frac{m}{s})$ are the angular and linear (tangential) velocities respectively. According to Fig. 1, it can be concluded that with the rotation of an object at a certain angular velocity around the center of rotation, a gravitational acceleration will occur that could be equal to $g = 9.806\frac{m}{s^2}$. According to the acceleration equation $a = r\omega^2$, it can be concluded that by selecting the appropriate angular velocity at a specific orbit, a gravitational acceleration equal to the gravitational acceleration on the Earth's surface is created. Fig. 2 shows the relationship between the radius (R) and the rotational angular velocity ω (in terms of revolutions per minute $\frac{rev}{min}$) so that the obtained gravitational acceleration in the rotating doughnut will be equal to 9.806. Also, Fig. 3 demonstrates the equivalent tangential velocity (V_{Lin} $\frac{m}{s}$) for radius (r) changes.

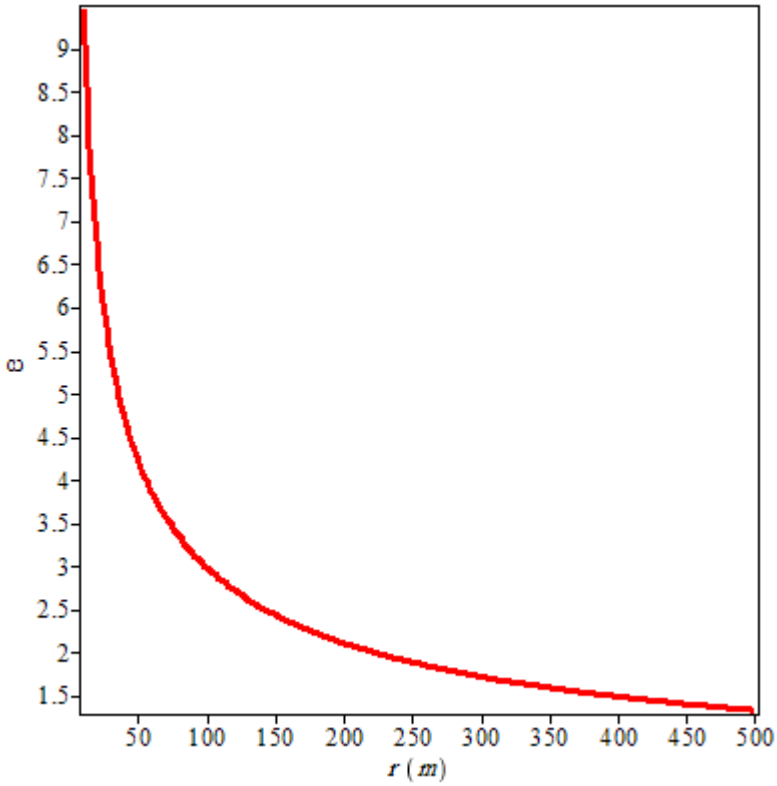

Fig. 2. Variation of angular velocity of a rotating doughnut ($\omega\ \frac{rev}{min}$) versus the radius of rotation (r)

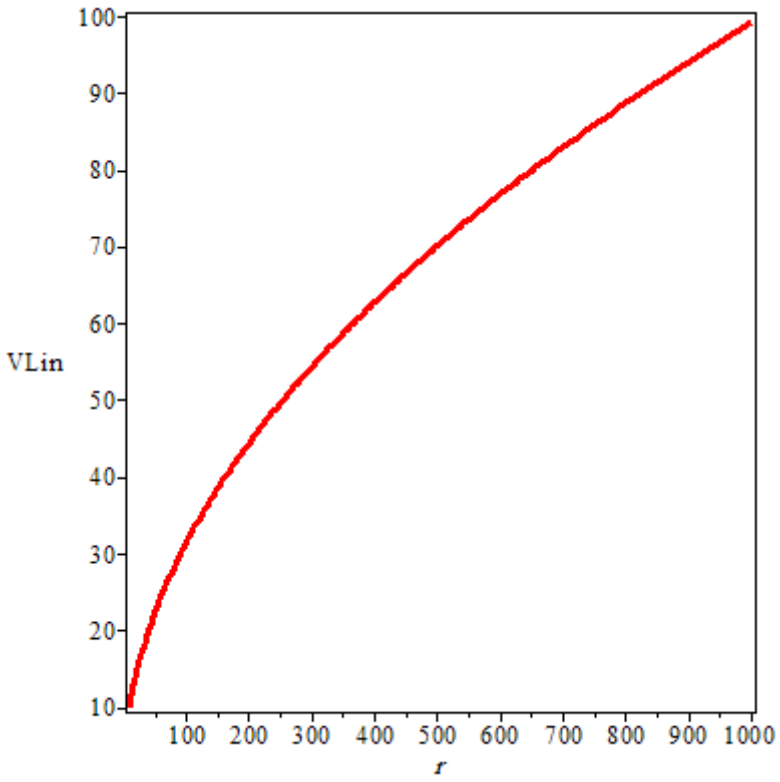

Fig. 3. Tangential velocity (V_{Lin} $\frac{m}{s}$) due to the respected radius change

It is observed that (Fig. 2) whatever the radius increases the angular velocity which is required for constant amount of gravitational acceleration equal to $g = 9.806\frac{m}{s^2}$ decreases, however, the variation is nonlinear with descending slope. Figs. 2 and 3 give theoretical information in regard to the suitable radius (r) and angular velocity (ω) for providing $g = 9.806\frac{m}{s^2}$ on the rotating vehicle. However, there are some physical limitations for r and ω. For example, high amounts of V_{Lin} and ω causes serious health problem and inconvenient for astronauts. The appropriate ω is in the range of $\omega \leq 10\frac{rev}{min}$. In the scale of huge space stations, the large amount of radius is expected. According to Fig. 2, if the radius of doughnut-shape space station is equal to 1000 meters, the angular velocity should be about $1\frac{rev}{min}$, however, the tangential velocity will be $V_{Lin} = 100\frac{m}{s}$ or 360 $\frac{km}{hr}$ which is too high. Consequently, it is

preferred to create for example 70 percentage of $g = 9.806 \frac{m}{s^2}$ that causes a reduction in needed angular velocity and in therefore V_{Lin}.

3. Space accommodation and challenges

As mentioned earlier, the lack of gravity in long-distance space travel will cause serious physical problems for astronauts. Fig. 4 shows a space station with two places for astronauts to live. The first part is a rotating cylindrical structure and the second part is a torus structure rotating around the central axis. In this study, two structures, a cylindrical and a torus one, have been studied in terms of mechanical forces that cause deformation and stress in the body of the structure. In the previous section, it was explained under what conditions a gravitational force can occur in a structure under rotation equal to what is felt on the Earth's surface. The conditions that prevail in space are very different from the environmental conditions on the Earth's surface. For example, in space outside the Earth's atmosphere, the external imposed pressure on the spacecraft's surface is zero. But inside the spacecraft, a pressure of about $10^5 Pa$ must be created, which is felt on the surface of the Earth. Also, considerations related to astronauts' normally breathing should be considered. In addition, the temperature inside the spacecraft must be set to the same pleasant temperature as the Earth's surface. Similar to the discussion of temperature, considerations must be given to proper humidity inside the spacecraft. Therefore, in this study, the effects related to the hygro-thermal environment in the mechanical simulation have been considered to make the obtained results more reliable. In general, by knowing the stresses established in the structure of the spacecraft as well as the deformations created in it, it is possible to make more appropriate decisions about the use of suitable materials in the structure of the spacecraft. In this study, for the first time, the use of functionally graded materials (FGM) in the structure of spacecraft has been studied. Functionally graded materials are relatively new materials that are used in sensitive industries today [21-37]. Therefore, the

space industry will not be an exception to this rule, and structures made of FGM can be substituted instead of the common materials used so far in the structure of space crafts. Moreover, there are other metamaterials that would be appropriate choices for the future of space industries [38-41]. Consequently, the present study can be a good reference for researchers who will study in this field (mechanical analysis of space crafts) and are looking for a suitable alternative to the common materials used in space structures. In the following sections, the dynamic governing equations of the cylindrical and torus rotating structures made of functionally graded materials will be explained in detail.

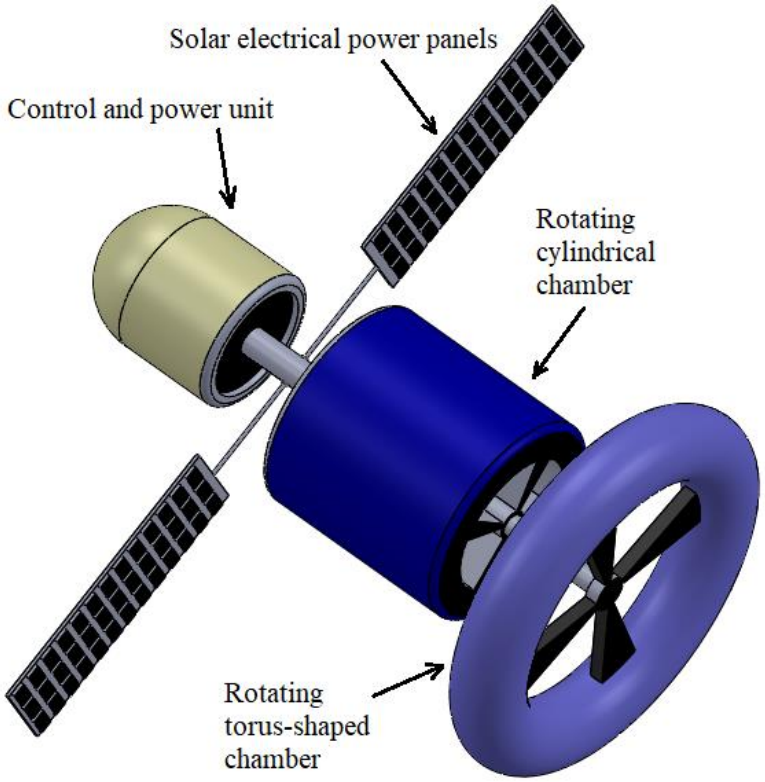

Fig. 4. Spacecraft with two rotating cylindrical and torus living chambers

4. Mechanical simulation of space chambers

4.1. Definition of geometries

In this section, the dynamic governing equations of a rotating cylinder [42-46] and torus [20] structures will be obtained. A schematic view of a slice of a doughnut as well as a rotating

cylinder are shown in Fig. 5a and 5b, respectively. The doughnut-shaped structure with thickness h, the radius of torus R_d, and the radius of tube R is under mechanical load q_z and heat-humidity loads with the difference in temperature ΔT and moisture percentage ΔH. The parameters related to the cylindrical structure are similar to the doughnut-shaped structure (Fig. 5a). It is worth noting to state that for analysis of both geometries, the internal pressure is applied circumferentially. According to Fig. 5, the conversion of a Cartesian coordinate system to cylindrical and torus coordinate systems can be defined based on the following equations:

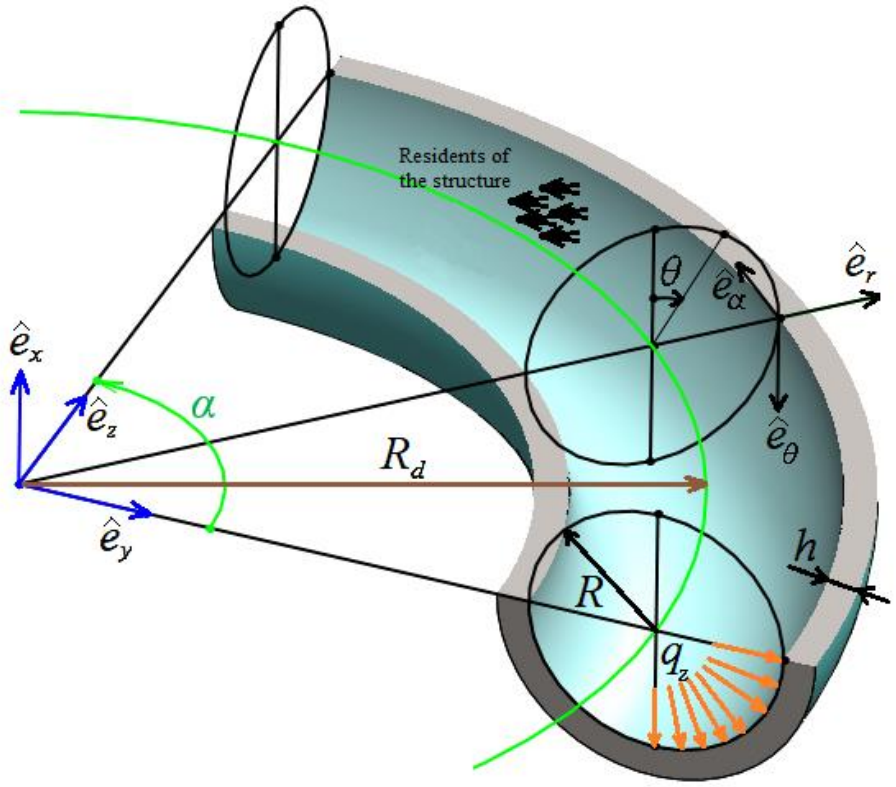

(a)

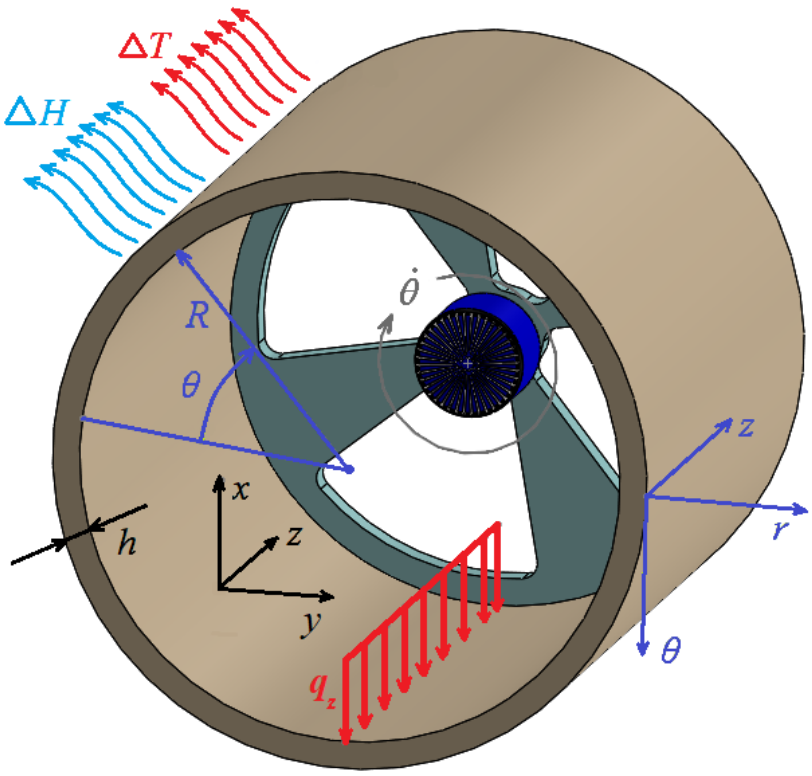

(b)

Fig. 5. Schematic view of (a) Torus (b) Cylindrical space structures

$$\text{Torus coordinates}\begin{cases} x = R\,cos(\theta) \\ y = (R_d + R\,sin(\theta))\,cos(\alpha) \\ z = (R_d + R\,sin(\theta))\,sin(\alpha) \end{cases} \quad \text{Cylindrical coordinates}\begin{cases} x = R\,cos(\theta) \\ y = R\,sin(\theta) \\ z = z \end{cases} \tag{1}$$

By performing mathematical calculations, the gradient vector (∇) in torus and cylindrical coordinate systems can be defined as follows:

$$\nabla_{\text{Torus}} = \left[\frac{\partial}{\partial r} \quad \frac{1}{R}\frac{\partial}{\partial \theta} \quad \frac{1}{(R_d + R\,sin(\theta))}\frac{\partial}{\partial \alpha}\right], \quad \nabla_{\text{Cylinder}} = \left[\frac{\partial}{\partial r} \quad \frac{1}{R}\frac{\partial}{\partial \theta} \quad \frac{\partial}{\partial z}\right] \tag{2}$$

Also, the conversion of the unit vectors in the cylindrical and torus coordinate systems to the Cartesian coordinate system will be according to the following equations:

$$\text{Torus}\begin{cases}\widehat{e_r} = \widehat{e_y}(cos(\theta)) + \widehat{e_y}(sin(\theta)\,cos(\alpha)) + \widehat{e_z}(sin(\theta)\,sin(\alpha)) \\ \widehat{e_\theta} = \widehat{e_x}(-sin(\theta)) + \widehat{e_y}(cos(\theta)\,cos(\alpha)) + \widehat{e_z}(cos(\theta)\,sin(\alpha)) \\ \widehat{e_\alpha} = \widehat{e_y}(-sin(\alpha)) + \widehat{e_z}(cos(\alpha))\end{cases}$$

$$\text{Cylinder}\begin{cases}\widehat{e_r} = \widehat{e_x}(cos(\theta)) + \widehat{e_y}(sin(\theta)\,cos(\alpha)) + \widehat{e_z}(sin(\theta)\,sin(\alpha)) \\ \widehat{e_\theta} = \widehat{e_x}(-sin(\theta)) + \widehat{e_y}(cos(\theta)\,cos(\alpha)) + \widehat{e_z}(cos(\theta)\,sin(\alpha)) \\ \widehat{e_z} = \widehat{e_z}\end{cases} \quad (3)$$

Since the purpose of this study is to investigate the dynamic behavior of the structure, the analysis of the velocity and acceleration of the structure should also be considered. According to the above equations, acceleration can be formulated in two systems of cylindrical and torus according to the following equations ($\dot{\theta} = \frac{d\theta}{dt}, \ddot{\theta} = \frac{d^2\theta}{dt^2}, \alpha = \frac{d\alpha}{dt}, \ddot{\alpha} = \frac{d^2\alpha}{dt^2}$)

$$\text{Torus}\begin{cases}a_r = \ddot{r} - r\dot{\theta}^2 - r\,sin^2(\theta)\,\dot{\alpha}^2 \\ a_\theta = r\ddot{\theta} + 2\dot{r}\dot{\theta} - r\dot{\theta}^2\,sin(\theta)\,cos(\theta) \\ a_\alpha = r\ddot{\alpha}\,sin(\theta) + 2\dot{r}\dot{\alpha}\,sin(\theta) + 2r\dot{\theta}\dot{\alpha}\,cos(\theta)\end{cases} \quad \text{Cylinder}\begin{cases}a_r = \ddot{r} - r\dot{\theta}^2 \\ a_\theta = r\ddot{\theta} + 2\dot{r}\dot{\theta} \\ a_z = \ddot{z}\end{cases} \quad (4)$$

4.2. Strain field

The tensor relation according to which the strains will be obtained in each system of assumed coordinates is introduced in general according to the following equation

$$\varepsilon = \frac{1}{2}[\nabla U + \nabla U^T + \nabla U \cdot \nabla U^T] \quad (5)$$

In the above equation, *U* will have three components in the assumed coordinate system and the operator ∇ is the gradient in the same coordinate system. In continue, the displacement field components will be obtained for the cylindrical coordinate system, and similar calculations can be performed to extract the strain field components in the torus coordinates. The *U* vector in the cylindrical coordinate system will be as follows:

$$\vec{U} = U_r\widehat{e_r} + U_\theta\widehat{e_\theta} + U_z\widehat{e_z} \quad (6)$$

Next, according to the definition of ∇ in the cylindrical coordinate system, the expansion of Eq. (5) can be rewritten as follow

$$\nabla U = \begin{bmatrix} \frac{\partial}{\partial r}\widehat{e_r} & \frac{1}{R}\frac{\partial}{\partial \theta}\widehat{e_\theta} & \frac{\partial}{\partial z}\widehat{e_z} \end{bmatrix} \begin{bmatrix} U_r\widehat{e_r} \\ U_\theta\widehat{e_\theta} \\ U_z\widehat{e_z} \end{bmatrix} = \begin{bmatrix} \frac{\partial U_r}{\partial r} & \frac{\partial U_\theta}{\partial r} & \frac{\partial U_z}{\partial r} \\ \frac{1}{R}\left(\frac{\partial U_r}{\partial \theta} - U_\theta\right) & \frac{1}{R}\left(\frac{\partial U_\theta}{\partial \theta} + U_r\right) & \frac{1}{R}\frac{\partial U_z}{\partial \theta} \\ \frac{\partial U_r}{\partial z} & \frac{\partial U_\theta}{\partial z} & \frac{\partial U_z}{\partial z} \end{bmatrix}$$

$$\nabla U^T = \begin{bmatrix} \frac{\partial U_r}{\partial r} & \frac{1}{R}\left(\frac{\partial U_r}{\partial \theta} - U_\theta\right) & \frac{\partial U_r}{\partial z} \\ \frac{\partial U_\theta}{\partial r} & \frac{1}{R}\left(\frac{\partial U_\theta}{\partial \theta} + U_r\right) & \frac{\partial U_\theta}{\partial z} \\ \frac{\partial U_z}{\partial r} & \frac{1}{R}\frac{\partial U_z}{\partial \theta} & \frac{\partial U_z}{\partial z} \end{bmatrix} \tag{7}$$

In Eq. (5), it should be noted that the expression $\nabla U \cdot \nabla U^T$ will represent the nonlinear part of the strain field, which is usually omitted due to a significant increase in the number of calculations. But sometimes this nonlinear expression cannot be ignored and ignoring it will cause serious errors in the numerical results. For example, if the mechanical load on the structure is high and the deformation of the structure occurs in the range of large deformations, the mentioned nonlinear expression must also be considered. Of course, if it is aimed to find the maximum deformation in direction of the applied loading, von Kármán's assumptions can be considered to simplify the extracted equations in order to obtain large deformations. Therefore, the final shape of the nonlinear strain field in the cylindrical coordinate system is formulated as a strain tensor below. It should be noted that the strain field tensor is symmetric or in other words the relation $\sigma_{ij} = \sigma_{ji}$ will be established. Also, the strain created by hygro-thermal effect is implemented in total strain tensor. Parameters α_T and β are the thermal expansion and moisture coefficients respectively,

$$\varepsilon_{ij} = \begin{bmatrix} \varepsilon_{rr} & \varepsilon_{r\theta} & \varepsilon_{rz} \\ \varepsilon_{\theta r} & \varepsilon_{\theta\theta} & \varepsilon_{\theta z} \\ \varepsilon_{zr} & \varepsilon_{z\theta} & \varepsilon_{zz} \end{bmatrix} - (\alpha_T \Delta T + \beta \Delta H) \begin{bmatrix} 1 & 0 & 0 \\ 0 & 1 & 0 \\ 0 & 0 & 1 \end{bmatrix}$$

$$\varepsilon_{rr} = \left(\frac{\partial U_r}{\partial r}\right) + \frac{1}{2}\left(\frac{\partial U_r}{\partial r}\right)^2$$

$$2\varepsilon_{r\theta} = 2\varepsilon_{\theta r} = \frac{1}{R}\left(\frac{\partial U_r}{\partial \theta} - U_\theta\right) + \left(\frac{\partial U_\theta}{\partial r}\right) + \frac{1}{R}\left(\frac{\partial U_r}{\partial r}\right)\left(\frac{\partial U_r}{\partial \theta}\right)$$

$$2\varepsilon_{rz} = 2\varepsilon_{zr} = \left(\frac{\partial U_r}{\partial z} + \frac{\partial U_z}{\partial r}\right)$$

$$\varepsilon_{\theta\theta} = \frac{1}{R}\left(\frac{\partial U_\theta}{\partial \theta} + U_r\right) + \frac{1}{2R^2}\left(\left(\frac{\partial U_r}{\partial \theta}\right)^2 + U_r^2\right)$$

$$2\varepsilon_{\theta z} = 2\varepsilon_{z\theta} = \frac{1}{R}\frac{\partial U_z}{\partial \theta} + \frac{\partial U_\theta}{\partial z}$$

$$\varepsilon_{zz} = \frac{\partial U_z}{\partial z} \tag{8}$$

4.3. Extraction of dynamic equations of the cylindrical structure

There are many advantages of using the principle of minimum potential energy to obtain the governing equations. One of them is the achievement of boundary conditions simultaneously with the derivation of the governing equations. According to the principle of minimum potential energy, the energy variations of the whole set should be equal to zero. The general equation of this theory is as follows

$$\delta\Pi = \delta U_\varepsilon + \delta K_{ken} + \delta F_{ext} = 0$$

$$\delta U_\varepsilon = \int_0^t \left(\iiint_V \sigma_{ij}\delta\varepsilon_{ij}\right) dt \quad i,j = r,\theta,z \quad (\text{V is the volume})(dV = Rdrd\theta dz)$$

$$\delta K_{ken} = -\frac{\delta}{2}\int_0^t \left(\iiint_V \rho\left(\left(\frac{\partial U_r}{\partial t}\right)^2 + \left(\frac{\partial U_\theta}{\partial t}\right)^2 + \left(\frac{\partial U_z}{\partial t}\right)^2\right) dV\right) dt$$

$$\delta F_{ext} = \int_0^t \left(-\iint_A q_z(\delta U_r) dA\right) dt \qquad (\text{A is the area})(dA = Rd\theta dz) \tag{9}$$

In the above equation, δU_ε, δK_{ken} and δF_{ext} are the variation in strain energy, kinetic energy and work performed by external loads in the system. σ_{ij} is the stress created in the structure that will be obtained according to Hooke's law ($\sigma_{ij} = C : \varepsilon_{ij}$).

Matrix *C* is the stiffness matrix of the material used, which in this study, the employed structure is considered as a functionally graded material (FGM). Recently, the use of FG materials is increased, but their manufacturing process is still a serious challenge. The aerospace industry needs to be progressed by using new and high-tech instruments and materials. So, the use of FG materials in the aerospace industry can be studied by researchers due to their special and unique properties. The mechanical properties of FGMs change in one or more different directions and their value will vary from the initial value to the secondary value. For example, the definition of Young's modulus ($E(r)$) can be formulated as an equation with changes in the structure thickness from E_1 to E_2. Parameter g defines the intensity of the rate of changes from E_1 to E_2. The more value of parameter g, the rate of changes from E_1 to E_2 will be increased,

$$C = \frac{E(r)}{1-\left(\nu(r)\right)^2}\begin{bmatrix} 1 & \nu(r) & 0 & 0 & 0 & 0 \\ \nu(r) & 1 & 0 & 0 & 0 & 0 \\ 0 & 0 & \frac{1-\nu(r)}{2} & 0 & 0 & 0 \\ 0 & 0 & 0 & \frac{1-\nu(r)}{2} & 0 & 0 \\ 0 & 0 & 0 & 0 & \frac{1-\nu(r)}{2} & 0 \\ 0 & 0 & 0 & 0 & 0 & \frac{1-\nu(r)}{2} \end{bmatrix}$$

$$E(r) = (E_1 - E_2)\left(\frac{r}{h}+\frac{1}{2}\right)^g + E_2; \nu(r) = (\nu_1 - \nu_2)\left(\frac{r}{h}+\frac{1}{2}\right)^g + \nu_2 \quad \left(-\frac{h}{2} \le r \le \frac{h}{2}\right) \qquad (10)$$

As the energy equations have been extracted before, it is observed that the displacement components based on the cylindrical coordinate system are considered as general expressions U_r, U_θ and U_z. Here these components can be selected so that the results are more in line with reality and at the same time the calculations are reduced to a minimum. One of the popular displacement field theories that, while simple in equations, provides good results in the mechanical analysis of structures is Mindlin's first-order shear deformation theory (FSDT). In this theory, three transfer displacement functions u_0, v_0 and w_0 as well as two rotation functions

ψ_1 and ψ_2 around the two axes z and θ are introduced. The FSDT displacement field equations are defined as follows:

$$U_\theta(r,\theta,z,t) = u_0(\theta,z,t) + r\psi_1$$
$$U_z(r,\theta,z,t) = v_0(\theta,z,t) + r\psi_2(\theta,z,t)$$
$$U_r(r,\theta,z,t) = w_0(\theta,z,t) \tag{11}$$

The variable r indicates changes in the thickness direction. As can be seen, the changes U_r, U_θ and U_z are defined linearly. The application of the FSDT theory provides suitable results for relatively thick structures. Space structures are in the range of medium thicknesses, so it is predicted to provide good results using this theory.

By applying the FSDT displacement field in the energy equations, their expansion will be rewritten as the following equations

$$\begin{aligned}
\delta U_\varepsilon &= \int_0^t \Bigg(\iiint_V (\sigma_{rr}\delta\varepsilon_{rr} + \sigma_{r\theta}\delta\varepsilon_{r\theta} + \sigma_{rz}\delta\varepsilon_{rz} + \sigma_{\theta r}\delta\varepsilon_{\theta r} + \sigma_{\theta\theta}\delta\varepsilon_{\theta\theta} + \sigma_{\theta z}\delta\varepsilon_{\theta z} \\
&+\sigma_{zr}\delta\varepsilon_{zr} + \sigma_{z\theta}\delta\varepsilon_{z\theta} + \sigma_{zz}\delta\varepsilon_{zz})dV\Bigg)dt \\
&= \int_0^t \left(\iiint_V (\sigma_{rr}\delta\varepsilon_{rr} + \sigma_{zz}\delta\varepsilon_{zz} + \sigma_{\theta\theta}\delta\varepsilon_{\theta\theta} + 2\sigma_{r\theta}\delta\varepsilon_{r\theta} + 2\sigma_{rz}\delta\varepsilon_{rz} + 2\sigma_{\theta z}\delta\varepsilon_{\theta z})\, dV \right) dt \\
&= \int_0^t \Bigg(\int_0^L \int_0^\theta \int_{-\frac{h}{2}}^{\frac{h}{2}} \Bigg(\sigma_{zz} \left(\frac{\partial\delta v_0}{\partial z} + r\frac{\partial\delta\psi_2}{\partial z} + \left(\frac{\partial\delta w_0}{\partial z}\right)\left(\frac{\partial w_0}{\partial z}\right) \right) + \sigma_{\theta\theta} \left(\frac{1}{R}\left(\frac{\partial\delta u_0}{\partial\theta} + r\frac{\partial\delta\psi_1}{\partial\theta} + \delta w_0 \right) \right. \\
&+ \left. \frac{1}{R^2}\left(\left(\frac{\partial\delta w_0}{\partial\theta}\right)\left(\frac{\partial w_0}{\partial\theta}\right) + w_0\delta w_0 \right) \right) + \sigma_{z\theta} \left(\frac{1}{R}\left(\frac{\partial\delta v_0}{\partial\theta} + r\frac{\partial\delta\psi_2}{\partial\theta} \right) + \left(\frac{\partial\delta u_0}{\partial z} + r\frac{\partial\delta\psi_1}{\partial z} \right) \right. \\
&+ \left. \frac{1}{R}\left(\left(\frac{\partial\delta w_0}{\partial\theta}\right)\left(\frac{\partial w_0}{\partial z}\right) + \left(\frac{\partial w_0}{\partial\theta}\right)\left(\frac{\partial\delta w_0}{\partial z}\right) \right) \right) + \sigma_{rz}\left(\frac{\partial\delta w_0}{\partial z} + \delta\psi_2 \right) + \sigma_{r\theta}(\delta\psi_1 \\
&+ \left. \frac{1}{R}\left(\frac{\partial\delta w_0}{\partial\theta} - \delta u_0 - r\delta\psi_1 \right) \right) \Bigg) Rdrdzd\theta \Bigg) dt
\end{aligned} \tag{12}$$

$$\delta K_{ken} = -\frac{\delta}{2}\int_0^t \left(\iiint_V \rho \left(\left(\frac{\partial U_\theta}{\partial t}\right)^2 + \left(\frac{\partial U_z}{\partial t}\right)^2 + \left(\frac{\partial U_r}{\partial t}\right)^2 \right) dV \right) dt$$

$$= -\int_0^t \left(\iiint_V \rho \left(\left(\frac{\partial U_\theta}{\partial t}\frac{\partial\delta U_\theta}{\partial t}\right) + \left(\frac{\partial U_z}{\partial t}\frac{\partial\delta U_z}{\partial t}\right) + \left(\frac{\partial U_r}{\partial t}\frac{\partial\delta U_r}{\partial t}\right) \right) dV \right) dt =$$

$$= -\int_0^t \left(\iiint_V \rho \left(\left(\frac{\partial u_0}{\partial t} + r\frac{\partial \psi_1}{\partial t} \right) \left(\frac{\partial \delta u_0}{\partial t} + r\frac{\partial \delta \psi_1}{\partial t} \right) + \left(\frac{\partial v_0}{\partial t} + r\frac{\partial \psi_2}{\partial t} \right) \left(\frac{\partial \delta v_0}{\partial t} + r\frac{\partial \delta \psi_2}{\partial t} \right) \right. \right.$$

$$\left. \left. + \left(\frac{\partial w_0}{\partial t} \frac{\partial \delta w_0}{\partial t} \right) \right) dV \right) dt = -\int_0^t \left(\iint_A \left(I_1 \left(\frac{\partial u_0}{\partial t} \frac{\partial \delta u_0}{\partial t} \right) + I_2 \left(\frac{\partial u_0}{\partial t} \frac{\partial \delta \psi_1}{\partial t} + \frac{\partial \psi_1}{\partial t} \frac{\partial \delta u_0}{\partial t} \right) \right. \right.$$

$$+ I_3 \left(\frac{\partial \psi_1}{\partial t} \frac{\partial \delta \psi_1}{\partial t} \right) + I_1 \left(\frac{\partial v_0}{\partial t} \frac{\partial \delta v_0}{\partial t} \right) + I_2 \left(\frac{\partial v_0}{\partial t} \frac{\partial \delta \psi_2}{\partial t} + \frac{\partial \psi_2}{\partial t} \frac{\partial \delta v_0}{\partial t} \right) + I_3 \left(\frac{\partial \psi_2}{\partial t} \frac{\partial \delta \psi_2}{\partial t} \right)$$

$$\left. \left. + I_1 \left(\frac{\partial w_0}{\partial t} \frac{\partial \delta w_0}{\partial t} \right) \right) R d\theta dz \right) dt \qquad (I_1, I_2, I_3) = \int_{-\frac{h}{2}}^{\frac{h}{2}} \rho(1, r, r^2) dr \tag{13}$$

$$\delta K_{accel} = -\int_0^t \left(\iiint_v \rho r \left((\ddot{\theta}) \delta U_\theta - (\dot{\theta}^2) \delta U_r \right) dV \right) dt$$

$$= -\int_0^t \left(\iint_A I_1 R \left((\ddot{\theta}) \delta u_0 - (\dot{\theta}^2) \delta w_0 \right) R d\theta dz \right) dt \tag{14}$$

By integrating in the direction of thickness (r) and defining the stress results as follows, the strain energy variations can be rewritten,

$$\begin{cases} (N_{zz}, N_{z\theta}, N_{\theta\theta}, N_{r\theta}, N_{rz}) = \int_{-\frac{h}{2}}^{\frac{h}{2}} (\sigma_{zz}, \sigma_{z\theta}, \sigma_{\theta\theta}, \sigma_{r\theta}, \sigma_{rz}) dr \\ (M_{zz}, M_{z\theta}, M_{\theta\theta}, M_{r\theta}) = \int_{-\frac{h}{2}}^{\frac{h}{2}} (\sigma_{zz}, \sigma_{z\theta}, \sigma_{\theta\theta}, \sigma_{r\theta}) r dr \end{cases} \tag{15}$$

$$\delta U_\varepsilon = \int_0^t \left(\int_0^L \int_0^\theta \left(N_{zz} \frac{\partial \delta v_0}{\partial z} + M_{zz} \frac{\partial \delta \psi_2}{\partial z} + N_{zz} \left(\frac{\partial \delta w_0}{\partial z} \right) \left(\frac{\partial w_0}{\partial z} \right) + \frac{N_{\theta\theta}}{R} \left(\frac{\partial \delta u_0}{\partial \theta} \right) + \frac{M_{\theta\theta}}{R} \left(\frac{\partial \delta \psi_1}{\partial \theta} \right) \right. \right.$$

$$\frac{N_{\theta\theta}}{R} (\delta w_0) + \frac{N_{\theta\theta}}{R^2} \left(\left(\frac{\partial \delta w_0}{\partial \theta} \right) \left(\frac{\partial w_0}{\partial \theta} \right) + w_0 \delta w_0 \right) + \frac{N_{z\theta}}{R} \left(\frac{\partial \delta v_0}{\partial \theta} \right) + \frac{M_{z\theta}}{R} \left(\frac{\partial \delta \psi_2}{\partial \theta} \right) + N_{z\theta} \left(\frac{\partial \delta u_0}{\partial z} \right)$$

$$+ M_{z\theta} \left(\frac{\partial \delta \psi_1}{\partial z} \right) + \frac{N_{z\theta}}{R} \left(\left(\frac{\partial \delta w_0}{\partial \theta} \right) \left(\frac{\partial w_0}{\partial z} \right) + \left(\frac{\partial w_0}{\partial \theta} \right) \left(\frac{\partial \delta w_0}{\partial z} \right) \right)$$

$$\left. \left. + N_{rz} \left(\frac{\partial \delta w_0}{\partial z} + \delta \psi_2 \right) + N_{r\theta} (\delta \psi_1) + \frac{N_{r\theta}}{R} \left(\frac{\partial \delta w_0}{\partial \theta} \right) - \frac{N_{r\theta}}{R} (\delta u_0) - \frac{M_{r\theta}}{R} (\delta \psi_1) \right) R dz d\theta \right) dt \tag{16}$$

Now, by calculating the integrals, some of which are integrals by part, and adding the corresponding values of δu_0, δv_0, δw_0, $\delta \psi_1$ and $\delta \psi_2$, the dynamic governing equations of space cylindrical structure (that rotates around the central axis) can be obtained below:

$$\delta u_0 : N_{r\theta} + \frac{\partial N_{\theta\theta}}{\partial \theta} + R\frac{\partial N_{z\theta}}{\partial z} + I_1 R^2 \ddot{\theta} - R\left(I_1 \frac{\partial^2 u_0}{\partial t^2} + I_2 \frac{\partial^2 \psi_1}{\partial t^2} \right) = 0 \tag{17}$$

$$\delta v_0: \frac{\partial N_{z\theta}}{\partial \theta} - R\frac{\partial N_{zz}}{\partial z} - R\left(I_1\frac{\partial^2 v_0}{\partial t^2} + I_2\frac{\partial^2 \psi_2}{\partial t^2}\right) = 0 \tag{18}$$

$$\delta w_0: \frac{\partial N_{r\theta}}{\partial \theta} - N_{\theta\theta} + R\frac{\partial N_{rz}}{\partial z} + \frac{1}{R}\frac{\partial}{\partial \theta}\left(N_{\theta\theta}\frac{\partial w_0}{\partial \theta}\right) - \frac{1}{R}(N_{\theta\theta}w_0) + \frac{\partial}{\partial \theta}\left(N_{z\theta}\frac{\partial w_0}{\partial z}\right)$$

$$+\frac{\partial}{\partial z}\left(N_{z\theta}\frac{\partial w_0}{\partial \theta}\right) + R\frac{\partial}{\partial z}\left(N_{zz}\frac{\partial w_0}{\partial z}\right) + Rq_z - I_1R^2\dot{\theta}^2 - I_1R\frac{\partial^2 w_0}{\partial t^2} = 0 \tag{19}$$

$$\delta \psi_1: M_{r\theta} - RN_{r\theta} + \frac{\partial M_{\theta\theta}}{\partial \theta} + R\frac{\partial M_{z\theta}}{\partial z} - R\left(I_2\frac{\partial^2 u_0}{\partial t^2} + I_3\frac{\partial^2 \psi_1}{\partial t^2}\right) = 0 \tag{20}$$

$$\delta \psi_2: \frac{\partial M_{z\theta}}{\partial \theta} - RN_{rz} + R\frac{\partial M_{zz}}{\partial z} - R\left(I_2\frac{\partial^2 v_0}{\partial t^2} + I_3\frac{\partial^2 \psi_2}{\partial t^2}\right) = 0 \tag{21}$$

To study several boundary conditions for the cylinderical structure, the following conditions are considered,

$$Clamped\ (C): u_0 = v_0 = w_0 = \psi_1 = \psi_2 = 0 \quad z = 0, L \tag{22}$$

$$Simply - supported\ (S): u_0 = v_0 = w_0 = \psi_1 = M_{zz} = 0 \quad z = 0, L \tag{23}$$

$$Free\ edge\ (F): N_{zz} = N_{z\theta} = N_{rz} = M_{zz} = M_{z\theta} = 0 \quad z = 0, L \tag{24}$$

If the cylindrical structure is uniform under mechanical loading and the environmental conditions (temperature and humidity) are evenly distributed throughout the structure, there will be no change in θ direction ($\frac{\partial}{\partial \theta}(f) = 0$). If the angular acceleration is omitted, or in other words $\dot{\theta} = 0$, the principle of uniformity of the dynamic load on the set is observed and $U_\theta = 0$ in the displacement field. This assumed principle is not far from reality. Because in practice, variable angular velocity will cause many problems on the health of the inhabitants of the space structure and will cause significant stress in structure and this category should be avoided as much as possible. As mentioned earlier, the angular velocity of the structure must be determined in a way that residents feel the equal gravitational force as on the Earth's surface. Finally, the displacement field will be rewritten simpler according to the following equations

$$\begin{cases} U_\theta(r,z,t) = 0 \\ U_z(r,z,t) = v_0(z,t) + r\psi_2(z,t) \\ U_r(r,z,t) = w_0(z,t) \end{cases} \tag{25}$$

As can be seen, the obtained equations of the space cylindrical structure (under uniform loading) is a set of nonlinear second-order partial differential equations as follow:

$$\delta v_0: \frac{\partial N_{zz}}{\partial z} + \left(I_1 \frac{\partial^2 v_0}{\partial t^2} + I_2 \frac{\partial^2 \psi_2}{\partial t^2}\right) = 0 \tag{26}$$

$$\delta w_0: R\frac{\partial N_{rz}}{\partial z} - N_{\theta\theta} - \frac{1}{R}(N_{\theta\theta} w_0) + R\frac{\partial}{\partial z}\left(N_{zz}\frac{\partial w_0}{\partial z}\right) + Rq_z - I_1 R^2 \dot{\theta}^2 - I_1 R \frac{\partial^2 w_0}{\partial t^2} = 0 \tag{27}$$

$$\delta \psi_2: N_{rz} - \frac{\partial M_{zz}}{\partial z} + \left(I_2 \frac{\partial^2 v_0}{\partial t^2} + I_3 \frac{\partial^2 \psi_2}{\partial t^2}\right) = 0 \tag{28}$$

4.4. Governing equations of the rotating doughnut-shaped structure

In the previous section, the dynamic equations of the structure of space cylinders were obtained using the principle of minimum energy. It is now possible to derive the governing equations for the doughnut-shaped structure as well. The procedure is the same as extracting the governing equations of the cylindrical structure, and the only thing to note is that there are changes in both α and θ directions (Fig. 5a), even if the mechanical and environmental loads are applied to the system uniformly. Assuming constant angular velocities ($\ddot{\alpha} = \ddot{\theta} = 0$), due to the special geometric shape of the doughnut, changes will occur in both directions and $\frac{\partial}{\partial \theta}(f)$ cannot be ignored like a cylindrical structure and also U_θ will no longer be equal to zero.

After applying the method similar to the previous section and considering the hypotheses expressed, finally (due to the avoidance of reprocessing) the nonlinear dynamic governing equations of the space doughnut-shaped structure that rotates around its central axis (axis *x* in Fig. 5a, also $\dot{\theta} = \ddot{\theta} = 0$) will be formulated as the following equations, which is a set of nonlinear third-order partial differential equations. The related solving process in doughnut-shaped structure is dramatically more complex than the cylindrical one,

$$\delta u_0: \frac{\partial N_{\alpha\alpha}}{\partial \alpha} + sin(\theta)\, Q_{r\alpha} + 2\, cos(\theta)\, N_{\theta\alpha} + \left(\frac{R_t}{R} + sin(\theta)\right)\frac{\partial N_{\theta\alpha}}{\partial \theta}$$

$$+(R_t + R\,sin(\theta))\left(\left(I_1\frac{\partial^2 u_0}{\partial t^2} + I_2\frac{\partial^2 \psi_1}{\partial t^2}\right)\right) = 0 \tag{29}$$

$$\delta v_0: \left(\frac{R_t}{R} + sin(\theta)\right) Q_{r\theta} + cos(\theta)\,(N_{\theta\theta} - N_{\alpha\alpha}) + \left(\frac{R_t}{R} + sin(\theta)\right)\frac{\partial N_{\theta\theta}}{\partial \theta} + \frac{\partial N_{\theta\alpha}}{\partial \alpha}$$

$$+(R_t + R\,sin(\theta))\left(I_1 R\ddot{\alpha}\,sin(\theta) + \left(I_1\frac{\partial^2 v_0}{\partial t^2} + I_2\frac{\partial^2 \psi_2}{\partial t^2}\right)\right) = 0 \tag{30}$$

$$\delta w_0: cos(\theta)\,Q_{r\theta} + \left(\frac{R_t}{R} + sin(\theta)\right)\frac{\partial Q_{r\theta}}{\partial \theta} + \frac{\partial Q_{r\alpha}}{\partial \alpha} - \left(\frac{R_t}{R} + sin(\theta)\right) N_{\theta\theta} - sin(\theta)\,N_{\alpha\alpha}$$

$$+\frac{1}{R}\frac{\partial}{\partial \theta}\left(\left(\frac{R_t}{R} + sin(\theta)\right) N_{\theta\theta}\frac{\partial N_{\theta\theta}}{\partial \theta}\right) - \frac{1}{R}\left(\frac{R_t}{R} + sin(\theta)\right) N_{\theta\theta} w_0 + \frac{1}{R}\frac{\partial}{\partial \theta}\left(N_{\theta\alpha}\frac{\partial w_0}{\partial \alpha}\right)$$

$$+\frac{1}{R}\frac{\partial}{\partial \alpha}\left(N_{\theta\alpha}\frac{\partial w_0}{\partial \theta}\right) + \frac{1}{R\left(\frac{R_t}{R} + sin(\theta)\right)}\frac{\partial}{\partial \alpha}\left(N_{\alpha\alpha}\frac{\partial w_0}{\partial \alpha}\right) - \frac{1}{R\left(\frac{R_t}{R} + sin(\theta)\right)}(N_{\alpha\alpha} w_0 (sin(\theta))^2)$$

$$+(R_t + R\,sin(\theta))\left(q_z - I_1 R\dot{\alpha}^2\,sin^2(\theta) + I_1\frac{\partial^2 w_0}{\partial t^2}\right) = 0 \tag{31}$$

$$\delta\psi_1: \frac{\partial M_{\alpha\alpha}}{\partial \alpha} - (R_t + R\,sin(\theta))Q_{r\alpha} + 2\,cos(\theta)\,M_{\theta\alpha} + \left(\frac{R_t}{R} + sin(\theta)\right)\frac{\partial M_{\theta\alpha}}{\partial \theta} + sin(\theta)\,M_{r\alpha}$$
$$+(R_t + R\,sin(\theta))\left(I_2\frac{\partial^2 u_0}{\partial t^2} + I_3\frac{\partial^2 \psi_1}{\partial t^2}\right) = 0 \tag{32}$$

$$\delta\psi_2: \left(\frac{R_t}{R} + sin(\theta)\right) M_{r\theta} + cos(\theta)\,(M_{\theta\theta} - M_{\alpha\alpha}) + (R_t + R\,sin(\theta))Q_{r\theta}$$
$$+\left(\frac{R_t}{R} + sin(\theta)\right)\frac{\partial M_{\theta\theta}}{\partial \theta} - \frac{\partial M_{\theta\alpha}}{\partial \alpha} + (R_t + R\,sin(\theta))\left(I_2\frac{\partial^2 v_0}{\partial t^2} + I_3\frac{\partial^2 \psi_2}{\partial t^2}\right) = 0 \tag{33}$$

The stress-moment resultants are defined in above equations as follows:

$$(N_{\alpha\alpha}, N_{\alpha\theta}, N_{\theta\theta}) = \int_{-\frac{h}{2}}^{\frac{h}{2}} (\sigma_{\alpha\alpha}, \sigma_{\alpha\theta}, \sigma_{\theta\theta})dr;\ (Q_{r\theta}, Q_{r\alpha}) = \int_{-\frac{h}{2}}^{\frac{h}{2}} (\sigma_{r\theta}, \sigma_{r\alpha})dr$$

$$(M_{\alpha\alpha}, M_{\alpha\theta}, M_{\theta\theta}, M_{r\theta}, M_{r\alpha}) = \int_{-\frac{h}{2}}^{\frac{h}{2}} (\sigma_{\alpha\alpha}, \sigma_{\alpha\theta}, \sigma_{\theta\theta}, \sigma_{r\theta}, \sigma_{r\alpha}) r dr \tag{34}$$

The result of differential equations obtained from a nonlinear analysis is very complex and sometimes unsolvable. There have been various methods available to facilitate the solution

of this model of equations. Hither we address this matter in the following based on the SAPM method tested and verified before [18-20, 27].

Moreover, the following boundary conditions are considered for the torus structure,

$$Clamped\ (C): u_0 = v_0 = w_0 = \psi_1 = \psi_2 = 0 \quad \alpha = 0, \alpha_T \tag{35}$$

$$Simply - supported\ (S): u_0 = v_0 = w_0 = \psi_1 = M_{\alpha\alpha} = 0 \quad \alpha = 0, \alpha_T \tag{36}$$

$$Free\ edge\ (F): N_{\alpha\alpha} = N_{\alpha\theta} = Q_{r\alpha} = M_{\alpha\alpha} = M_{\alpha\theta} = 0 \quad \alpha = 0, \alpha_T \tag{37}$$

5. Numerical results

5.1. Validation

To consider the reliability of the governing equations, it is necessary to dedicate this subsection. In this regard, with the help of the ABAQUS commercial program and take into account a typical cylindrical specimen, the results are tabulated according to Table 1. In so doing, we examine the following specifications for the aforesaid structure $E = 190GPa; \nu = 0.29; h = 0.01m; \dot{\theta} = 3rpm; R = 1m; L = 5m$.

Herein, two factors, namely the von Mises stress and the maximum deflection are estimated to attain the results whilst there are variations in the applied load. As mentioned earlier, we can convert the torus geometry into a cylindrical one in order to obtain the results of the cylinder structure.

Regarding the considered specifications for the cylinder structure, it is assumed that the torus radius (R_t) is infinite, in view of this, the $R_t = 10000\ m$ is employed. In the following the cylinder radius would be R = 1 *m* and the angle $\alpha = \frac{5}{10000}$ (rad) is utilized. Table 1 assesses both the aforementioned geometries, torus-shaped and cylindrical structures. It is observed the simulated cylinder which is originated from torus geometry gives almost similar results vis-a-vis the common cylinder. More importantly, the difference between the results of these two

cylindrical geometries is in good agreement with those of ABAQUS. In this way, the correctness of the governing equations, as well as the solving process, can be confirmed. Therefore, the problem can be developed further with high confidence.

Moreover, it can be seen that the increase of the internal pressure leads to an increase of the stress and the deformations. It is interesting to note that while the load reaches 0.4 *MPa*, the von Mises stress would be as same as the yield stress and thereupon, the structure will elastically fail and undesirably goes into the plastic region. Hence, the permissible limit for the value of internal pressure could be 0.4 *MPa* if we consider the assumed conditions on the problem.

Table 1. Validations for results the present article with ABAQUS for various values of loading.

q_z (MPa)	Present w (mm)		Present σ_{von} (MPa)		ABAQUS w (mm)	ABAQUS σ_{von} (MPa)
	Torus	Cylinder	Torus	Cylinder		
0.1	24.39	24.27	51.83	51.67	24.30	51.72
1	243.9	242.8	518.3	516.7	243.0	517.2
10	2439	2427	5183	5167	2430	5172

It may seem that the first comparison is not enough and further verification is required. In response to this problem, Table 2 is prepared through [47]. It is apparent that when the radius of the cylinder increases, the dimensionless deflections resulted from the reference and the present solution are going to be in the same amounts. The large difference between deflections obtained by the reference and current article can be seen for lower radiuses as well as the small amounts of g. In general, with the help of this tabulated comparison, one can approve the present solution particularly the present formulation which leads to considering the main problem of the work without any concern.

Table 2. Dimensionless displacement $\bar{w}$ for FGM cylinder.

$$\bar{w} = \frac{10^4 E_2}{q_z h (R/h)^4} w$$

g	R/h					
	4		10		100	
	[47]	Present	[47]	Present	[47]	Present
0.5	330.64	325.08	53.333	52.650	0.5213	0.5155
1	408.20	402.36	65.503	64.861	0.6391	0.6337
2	528.56	523.70	84.692	83.997	0.8257	0.8203

5.2. Nonlinear vs. linear analyses

First, it is momentous to present the differences in structural response in a nonlinear analysis compared with a linear one. This will aid us to know about the importance of nonlinear analysis for the considered structures. To obtain this, we intend to analyze cylindrical structure in both nonlinear and linear cases resulted in Figs. 6 and 7. In Fig. 6, one can observe the nondimensional deflection for the vertical axis and in the following for the horizontal axis the changes in the applied load. These states for Fig. 7 are respectively von Mises stress and also applied load. To make nondimensional deflection relation, we divide the dimensional deflection by the thickness. It should be noted that the loading is applied to the internal surface of the structure as an interior surface pressure. As it is seen by Fig. 6, when the values of deflections are more than those of thickness, it is significant that the analysis is linear or nonlinear and the linear study results are wrong for when the deflections amounts are further than the thickness values. On the other side, by looking at Fig. 7, one can see that while the amounts of the von Mises stress into the material of the cylinder are higher than 5 *GPa*, the linear analysis outcomes are going to be inaccurate. These two illustrated figures can entirely confirm the importance of the nonlinear analysis versus the linear one.

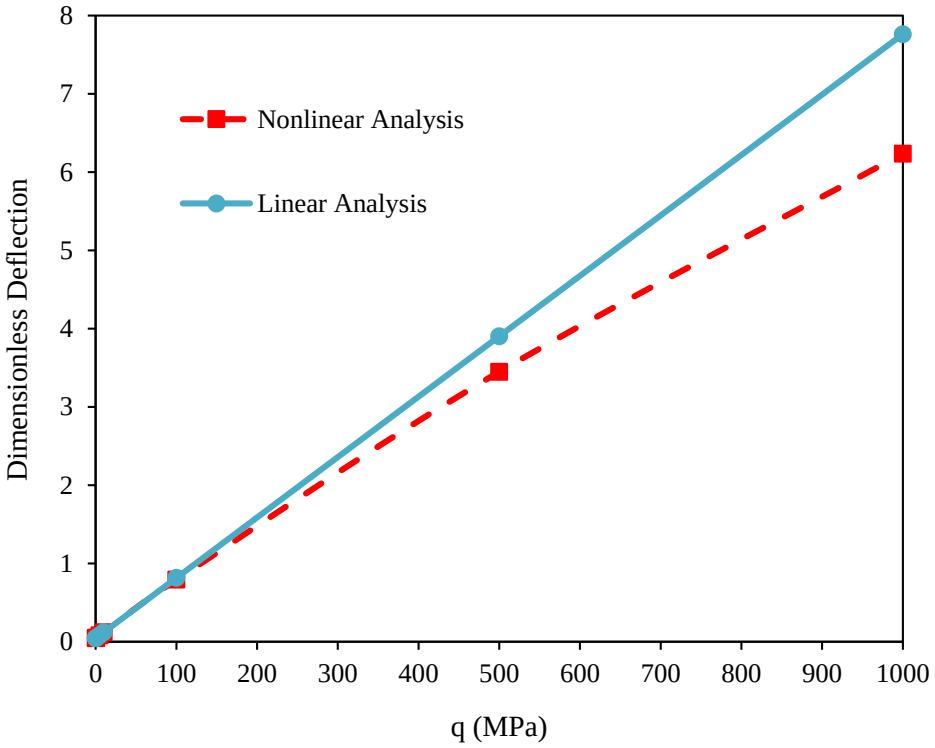

Fig. 6. Dimensionless deflection of the cylindrical structure vs. applied loading

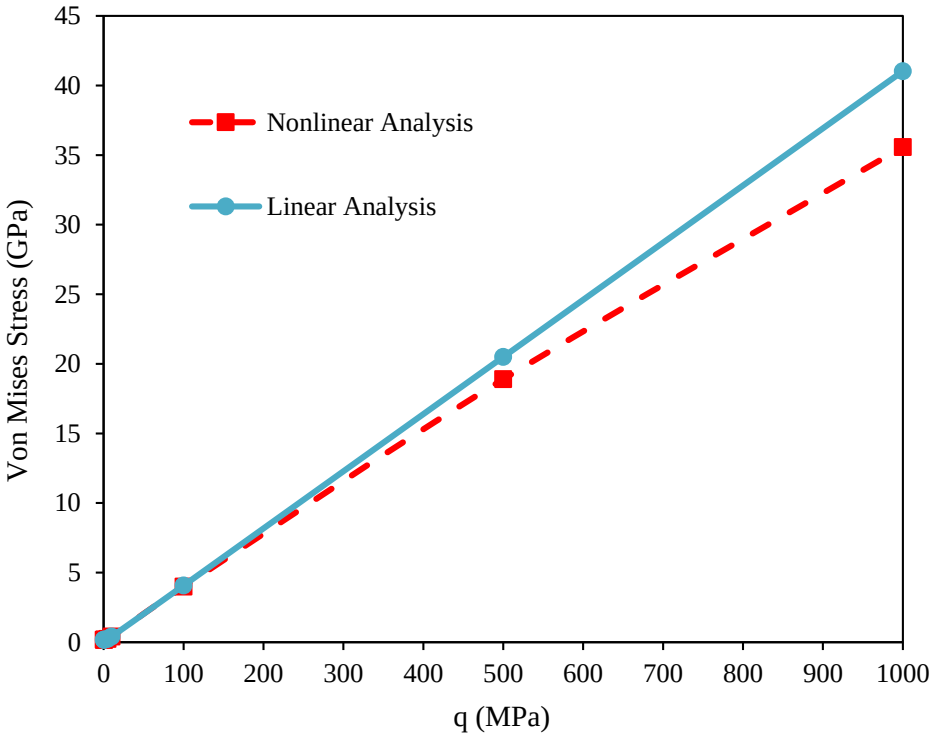

Fig. 7. von Mises stress into the cylindrical structure vs. applied loading

5.3. Study of effective parameters

As mentioned earlier, in this study two space structures with different geometric shapes, namely cylindrical and torus, have been investigated. The geometric shape of the torus has variations in both θ and α directions independently. As a result, the torus structure will not be like the cylindrical structure in which the change in the results is only in the θ-direction and constant (if the applied loads are constant). Even if the applied loads to the structure are constant, changes in the θ-direction must be considered for torus structures. Thus, the mechanical simulation of torus structures is more complex. Fig. 8 shows the deflection changes in the torus space structure with the following characteristics relative to the changes in the two variables θ and α.

$$R_d = 50m; R = 5m; E = 190GPa; \nu = 0.29; n = 4.23rpm; h = 0.1m \tag{38}$$

Note that the changes θ and α will be in the interval $0 < \alpha, \theta < 2\pi$. A schematic diagram of the torus structure under analysis can be seen in Fig. 5a. The changes in the direction of θ starts from the maximum value of about 60 *mm* and the trend of changes decreases up to $\theta = \pi$. Then from $\theta = \pi$ to $\theta = 2\pi$ the deflection (w) increases and at $\theta = 2\pi$ (which is actually the result as same for $\theta = \pi$) the deformation value will again be equal to 60 *mm*. It is observed that for $\theta = \frac{\pi}{2}, \frac{3\pi}{2}$ the value of w will be equal to zero. In this diagram, the initial value of angle α is approximately equal to zero and its final value is about 2π. Boundary conditions at these two edges are considered clamped. Depending on the characteristics of clamped end condition, it is predicted that the deflection value is equal to zero at $\alpha = 0, 2\pi$ and the maximum displacement occurs at the midpoint of the structure ($\alpha = \pi$). This situation can be seen in Fig. 8. A negative value of w means a deformation of the structure in the opposite direction to the applied load. Comparing the results of the torus and cylindrical structures, it can be concluded that the considerations related to the design of the structure in terms of its ability to withstand external

loads on the torus structure should be paid more attention. The oscillation of changes in the torus-shaped space structure is much greater than the cylindrical one. As a result, the complexity of the torus structure design is greater and it also has less capacity than the cylindrical structure for the long-term normal life of residents

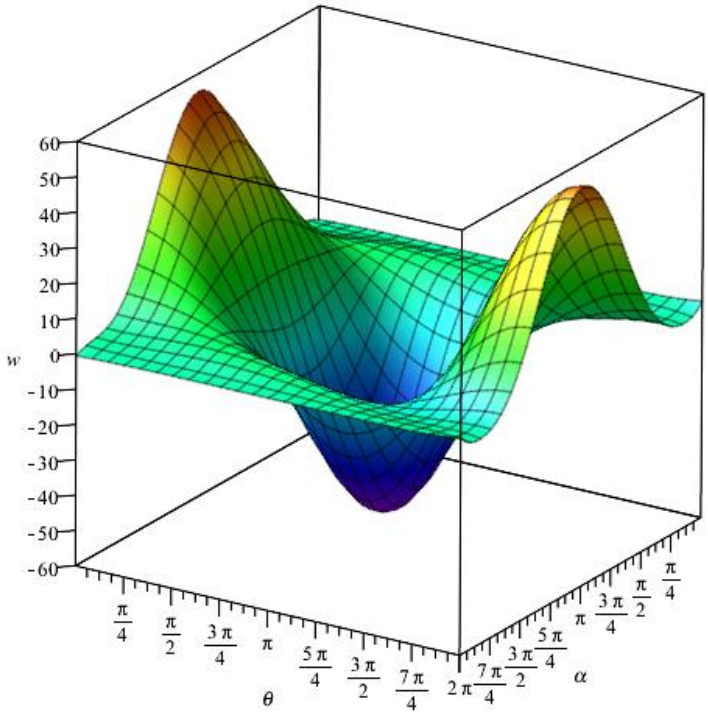

Fig. 8. Deflection (*w* in *mm*) of rotating torus-shaped structure in space due to α and θ directions

One of the most important issues that should be considered in the design of any instrument is the strength and bearing capacity of the designed structure against applied loads. The applied loads on the structure can be categorized as follows:

1) The internal uniform load caused by artificial pressure is equal to the atmospheric pressure on the Earth's surface. This pressure is estimated at about 100 kPa. At this pressure, residents no longer need to wear astronauts' clothing and will be able to wear normal clothing.

2) The pressure is caused by loads from residents and tools and equipment in the structure to the wall.
3) Centrifugal force due to the rotation of the structure around its central axis (to simulate and create gravitational acceleration equal to the acceleration of gravity on the Earth's surface about 9.806 $\frac{m}{s^2}$).
4) Stresses created due to environmental conditions due to the prevailing conditions of absolute vacuum in space, which should be considered temperature and humidity conditions similar to the Earth's surface for the normal life of space inhabitants.
5) Other effective loads that can cause stress in the structure, although their impact is small.

From the above-mentioned factors 1 to 4 are the cases whose effects have been studied. Also, the material of the structure has a very important effect on its resistance to applied loads. First, the effect of geometric factors on the strength of the structure will be investigated. Figs. 9 and 10 show the diagrams of maximum deflection and von Mises stresses of a cylindrical space structure with the following characteristics against uniform thickness changes of the structure, which are considered uniform for two different values of temperature changes ΔT = 0 and 50℃.

$$R = 25m; L = 100m; E = 190GPa; \nu = 0.29; n = 6rpm; \alpha_T = 1.73 \times 10^{-5} \quad (39)$$

It is well-known that a more rigid structure can be obtained with the increasing thickness of the structure. As can be seen from Figs. 9 and 10, as the thickness of the structure increases, the resistance to applied loads increases, and the stresses and deformations created in the structure decrease by an increment in the thickness of the structure. The slope of the changes at the beginning of the increase in thickness is very sharp and remarkable drop in stress and

deformation values is observed. However, from the thickness of approximately $h = 0.1\ m$ onwards, the slope of the changes is significantly reduced, and in practice, from a thickness of about $h = 0.2\ m$ onwards, the increase in thickness will no longer significantly change the deformation and the von Mises stress. Therefore, increasing the thickness of the structure will only increase the mass and consequently the cost of constructing the structure. Finding the appropriate thickness for a structure is a very important issue because choosing a small thickness will cause it to collapse against the applied loads and also choosing a high thickness will increase the cost of the project, which is uneconomical. So there is an ideal thickness that defines the boundary between the two explained conditions. Here, according to Fig 9, if a thickness of 5 *cm* is selected, the von Mises stress created in the structure will be equal to 60 *MPa* for temperature condition $\Delta T = 0$ and about 170 *MPa* for $\Delta T = 50℃$, which is less than the yield stress of the selected material (206 *MPa*). Another point that can be deduced from two diagrams (Figs. 9 and 10), is the significant effect of temperature difference on the strength of the structure. It is observed that increasing the temperature difference by about 50 degrees Celsius (50℃) will triple the stress and about six times increase the deformation of the structure, which is very considerable. Therefore, the effects of temperature on determining the strength of the structure are much more effective than the effects of applied mechanical loads. However, the behavior of the structure in the two cases of considering or not considering the temperature difference conditions is almost the same but with a very large difference in values. According to the characteristics of the structure and the results of Figs. 9 and 10 as the design point (without considering the safety factor), a thickness of 5 *cm* can be considered as the base thickness of the design.

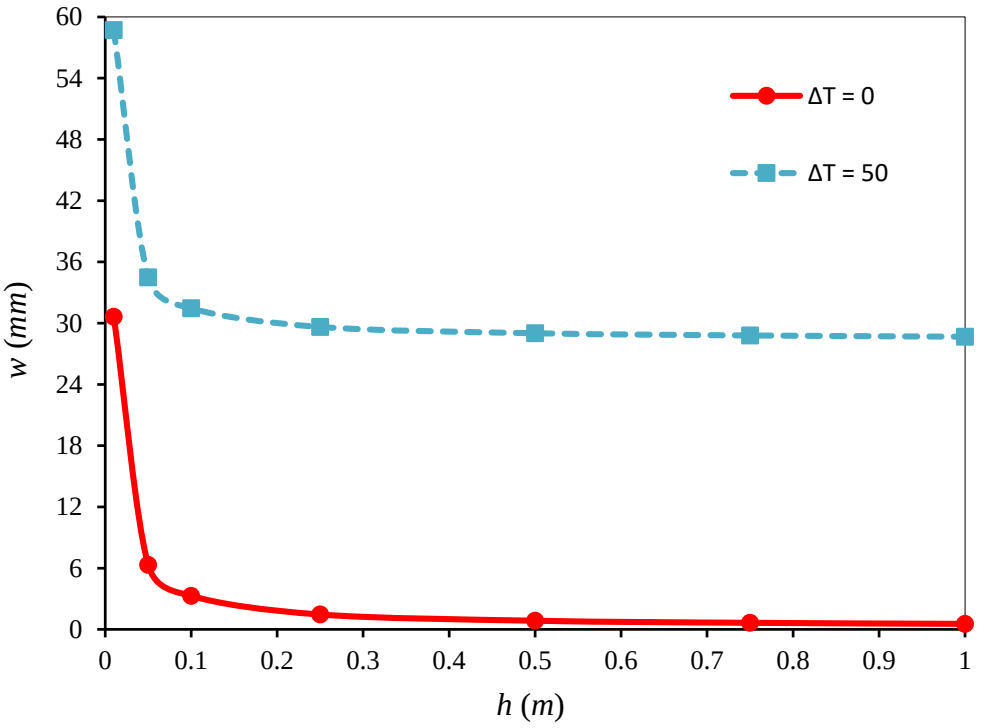

Fig. 9. Deformation variation versus thickness changes for different values of temperature differences

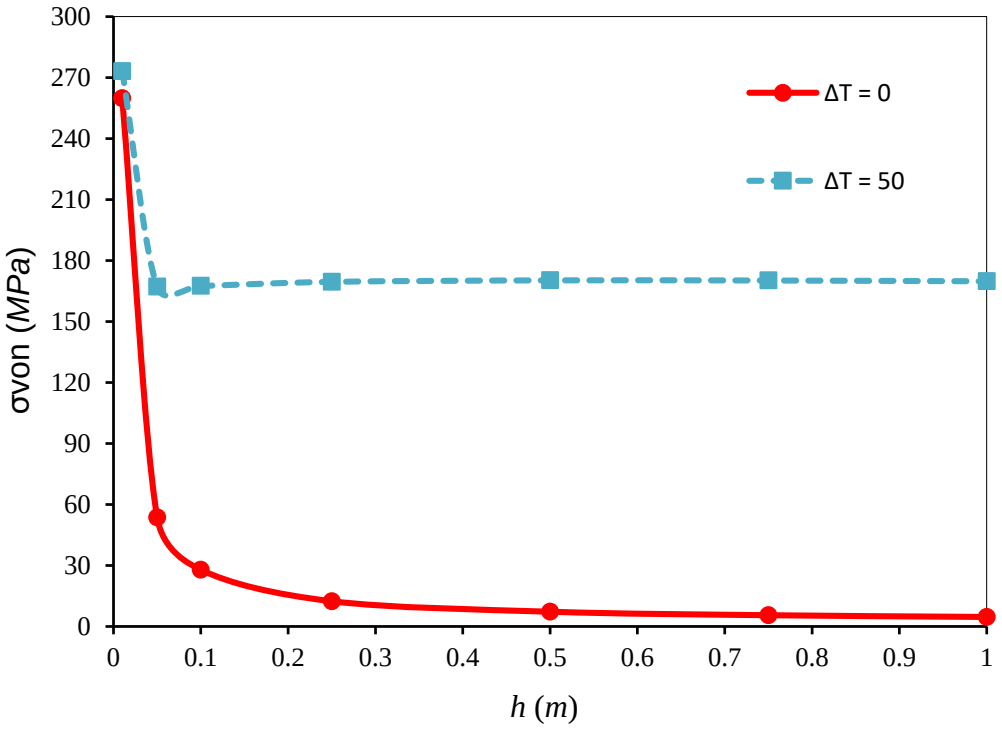

Fig. 10. von Mises stress variation versus thickness changes for different values of temperature differences

In Figs. 9 and 10, the effect of thickness on the strength of the structure was investigated. In a cylindrical structure, the three parameters of the structure radius, thickness, and length (height) determine the geometric dimensions. The higher the R and L, the more capacity the structure will have to accommodate residents and the equipment they need. In Figs. 11 and 12, the effect of the length of the space cylinder on the amount of deformation (w) and the stress of von Mises (σ_{von}) can be observed. The effects of temperature changes within the structure are also considered. According to Fig. 11, it is observed that at the beginning of the changes, the longer the length (L), the more the deformations in the structure will be (with a relatively upward slope). But only after a slight increase in L, its increase will no longer affect the results (deformation and von Mises stress). The initial rate of increase of the deformation for the increase of the L parameter for the case where temperature changes are considered (ΔT = 50℃) will be approximately equal to the other case (ΔT = 0). The shorter the length of the structure, the greater the effect of boundary conditions on the two edges of the beginning and end of the structure, and the less deformation will occur in the structure against the applied loads. However, with increasing L length, the effects of boundary conditions are reduced and the structure is less resistant to applied loads (mechanical and temperature) and as a result, the deformations increase. Of course, it should be noted that in this study, the loads applied to the structure are considered uniform. In Fig. 12, it is noteworthy that the temperature changes equal to zero (ΔT = 0) with increasing L, von Mises stress initially increased and then equalized to a fixed number. The resulting stress will not notice a considerable change in structure (as described in Fig. 11). However, in the case where the temperature change is equal to 50℃, it is observed that with increasing L von Mises stress has a downward trend (unlike the case ΔT =

0) and after reaching a certain value and then the changes will be uniform and similar. It can be argued that when L has a small amount (structure with small size), the effects of boundary conditions will increase the strength of the structure and the structure will be more resistant to deformation. But at the same time, there are thermal stresses in the structure, which can reduce its strength, and according to the trend of changes in Fig. 12, it can be concluded that thermal stresses have a significant effect, and due to the increase in L (because of the constant temperature difference and consequently thermal stresses) the effects of the structure's resistance to boundary conditions are reduced. In general, the result of these two parameters (thermal effects and size) will reduce the von Mises stress in the structure. However, this trend continues to converge to a certain value as the two effects reach equilibrium, as mentioned earlier. The general result of Figs. 11 and 12 can be stated that the length of the structure of space cylinders (L) has no effect on the strength of the structure and only by increasing it can create more capacity for residents and their needs. However, with the growth of L, the costs of the project will also increase.

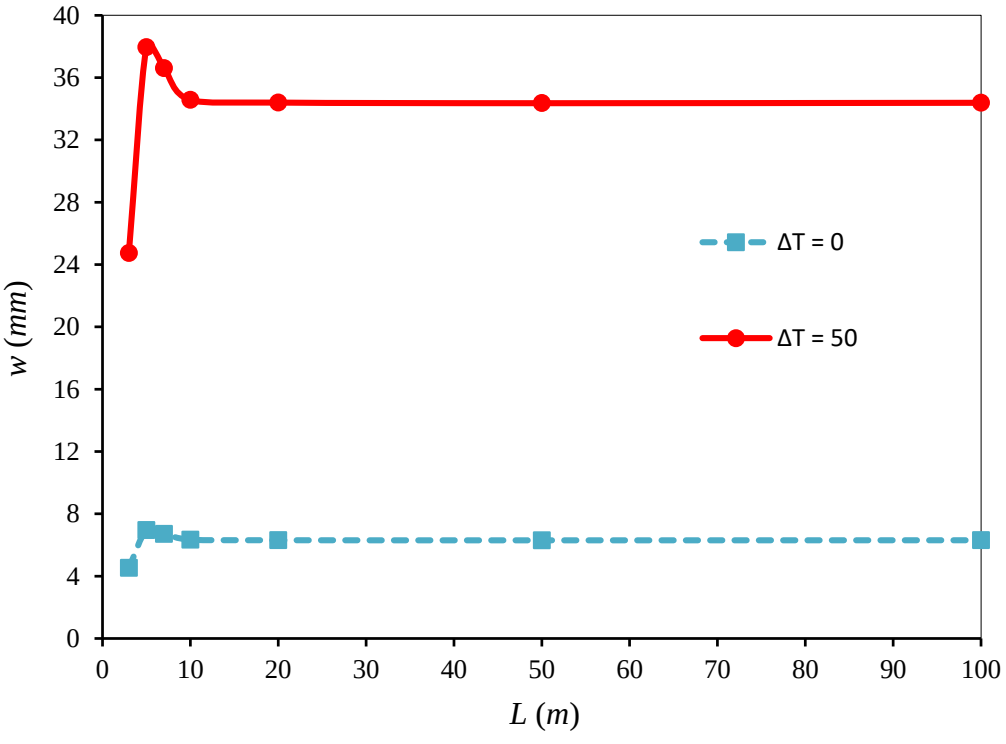

Fig. 11. Deflection changes due to increase of the length (L) of structure for different values of temperature differences

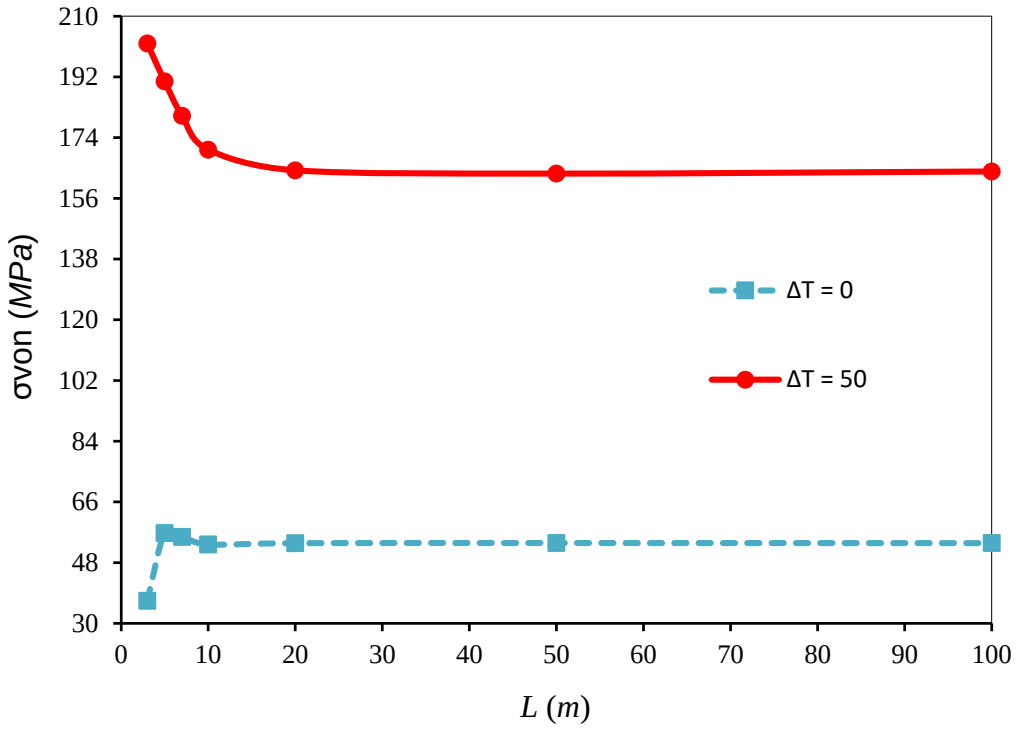

Fig. 12. von Mises changes due to increase of the length (L) of structure for different values of temperature differences

One of the most important issues that will make life comfortable and similar to the surface of the Earth in space is the existence of gravity, which has already been explained about its importance and how. In this section, the numerical results on the effects of simulated rotation and artificial gravity on the strength of the structure (in the form of two graphs of deflection and stress variation of the space structure) along the z-axis are investigated. The results are presented for different values of cylindrical structure radius and rotational angular velocity. There are 4 different values for the radius (R) and rotational angular velocity (n) according to the following values,

$$\begin{cases} R_1 = 25m \\ n_1 = 6rpm \end{cases}, \begin{cases} R_2 = 50m \\ n_2 = 4.23rpm \end{cases}, \begin{cases} R_3 = 75m \\ n_3 = 3.45rpm \end{cases}, \begin{cases} R_4 = 100m \\ n_4 = 3rpm \end{cases} \tag{40}$$

The values of R and n are calculated so that based on the selected radius R, the corresponding angular velocity is obtained in a way that the generated gravitational acceleration equal to 9.806 $\frac{m}{s^2}$ (according to the equation $g = R\left(\frac{2\pi n}{60}\right)^2$). As the values of R and n increase, the resulting deformation will increase. The upward trend of changes for both Figs. 13 and 14 will be ascending, although this is more evident for stress changes. Increasing the rotational angular velocity and radius of the structure will also reduce its strength. Because here the thickness of the structure is considered constant. In other words, as the radius of the structure increases, the $\frac{R}{h}$ ratio will increase (because h is assumed to be constant) and the so-called structure will weaken. Also, the structure angular rotation causes the creation of centrifugal forces and consequently, the dynamic load on the structure will be added to the static load (internal pressure). According to values R and n, it is observed that the changes in the rotational angular velocity are less than the structure radius. Therefore, the resulting dynamic centrifugal forces will not be very significant. Looking at Fig. 14, it can be seen that the amount of von Mises stress up to n_2 and R_2 is in the allowable range. But from now on, for n_3 and R_3, the von Mises stress generated in the structure will be approximately equal to the allowable yield stress point of the material, which causes insufficient uncertainty in the dimensions and design conditions of the structure. In the case of n_4 and R_4 conditions, the design is not acceptable at all and is rejected because σ_{von} has exceeded the allowable yield stress (206 MPa). The practical solution to this problem is to choose a structure with a smaller radius. If this is not possible and the size of the designed structure should be in the range of n_4 and R_4, some refines should be considered on other items that can be changed so that the structure can tolerate the loading conditions. One possible solution is to increase the thickness of the structure and examine the conditions analyzed in Figs. 9 and 10. In other words, by selecting the new thickness, the steps must be repeated for Figs. 9 and 10, and if validated, Figs. 13 and 14 should be redrawn for the

new conditions. If it is not possible to increase the thickness, the desired conditions can be achieved by reinforcing the material used in the structure or replacing it with a material capable of withstanding high loads. This issue will be analyzed in the continuation of the numerical discussion. But first, the subject that is briefly studied in Figs. 13 and 14 (the effect of angular rotation on the results) will be studied in more detail.

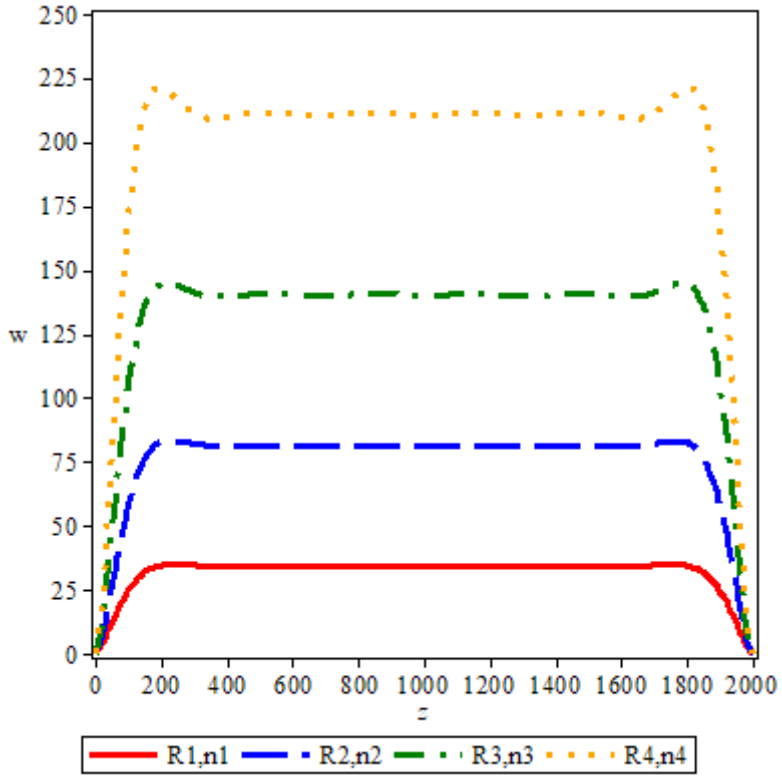

Fig. 13. Effect of radius and rotational speed of structure (R_i and n_i, i =1..4) on deflection versus z variations

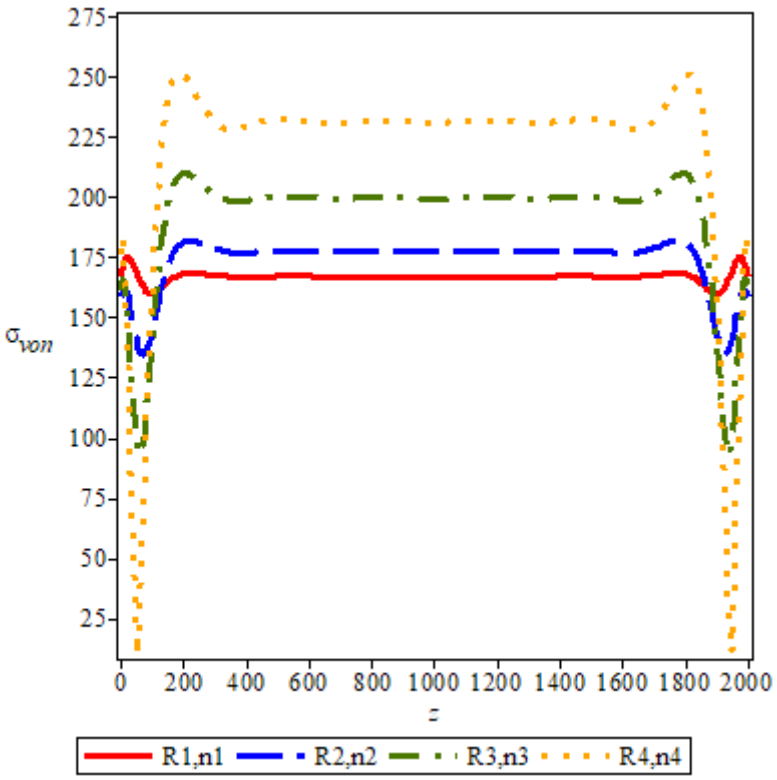

Fig. 14. Effect of radius and rotational speed of structure (R_i and n_i, i =1..4) on von Mises stress versus z variations

Increasing the rotational speed will reduce the strength of structure, which is shown in Figs. 15 and 16. The vertical axis parameters w_s and σ_s are two dimensionless parameters that are introduced as $w_s = \left(\frac{w_n}{w_0} - 1\right) \times 100$ and $\sigma_s = \left(\frac{\sigma_n}{\sigma_0} - 1\right) \times 100$. This ratio of deformation and stress in the case where the structure is rotating around a central axis with a certain rotational angular velocity (equal to n revolutions per minute) to deformation and stress in the case where the structure is stationary and without rotation (zero index). According to Figs. 15 and 16, as the angular velocity increases, the values of dimensionless deformation w_s and the dimensionless stress σ_s increase. The increase in w_s (Fig. 15) will be more significant than the increase in σ_s (Fig. 16). The two diagrams in Figs. 15 and 16 are plotted for three states without temperature changes (ΔT = 0), temperature changes equal to 50℃, and finally temperature changes equal to 100℃. It can be seen that the changes of w_s and σ_s with ΔT = 0 have the

highest growth rate, in which the rate of change has an upward trend and with increasing the angular velocity, the values of w_s and σ_s will grow significantly. In designing rotating space structures, it is tried to prevent unwanted rotational speeds. As can be seen in Figs. 15 and 16, high and unwanted rotational speeds will reduce the strength of the structure and there is a risk of its collapse and destruction in this case. Another result is that with increasing temperature changes (ΔT), the changes of w_s and σ_s are significantly reduced and no longer have a remarkable increase in the rate of deflection and stress of the structure as in the case of $\Delta T = 0$. Therefore, it can be concluded that if temperature effects are considered in the analysis, the effect of centrifugal forces due to the structure rotation will be reduced. For high-temperature differences (here ΔT = 100℃) even the effects of structural rotation can be ignored. For example, by increasing the rotational velocity from $n = 12$ *rpm* to $n = 24$ *rpm* for the mode $\Delta T = 0$, the dimensionless deformation of the structure will increase by about 5 times. But the same thing (w_s increment rate) is much lower for ΔT = 100℃. Increasing the angular velocity increases the centrifugal forces and makes residents of the space structure feel uncomfortable. Here (Figs. 15 and 16), an angular velocity equal to $n = 6$ *rpm* creates an artificial gravitational acceleration in a structure equal to the gravitational acceleration at the Earth's surface. Increasing the angular velocity increases the gravitational acceleration exponentially. Therefore, as mentioned earlier, this increase in the rotational velocity must be prevented so that both the strength of the structure and the normal life of the inhabitants are not endangered.

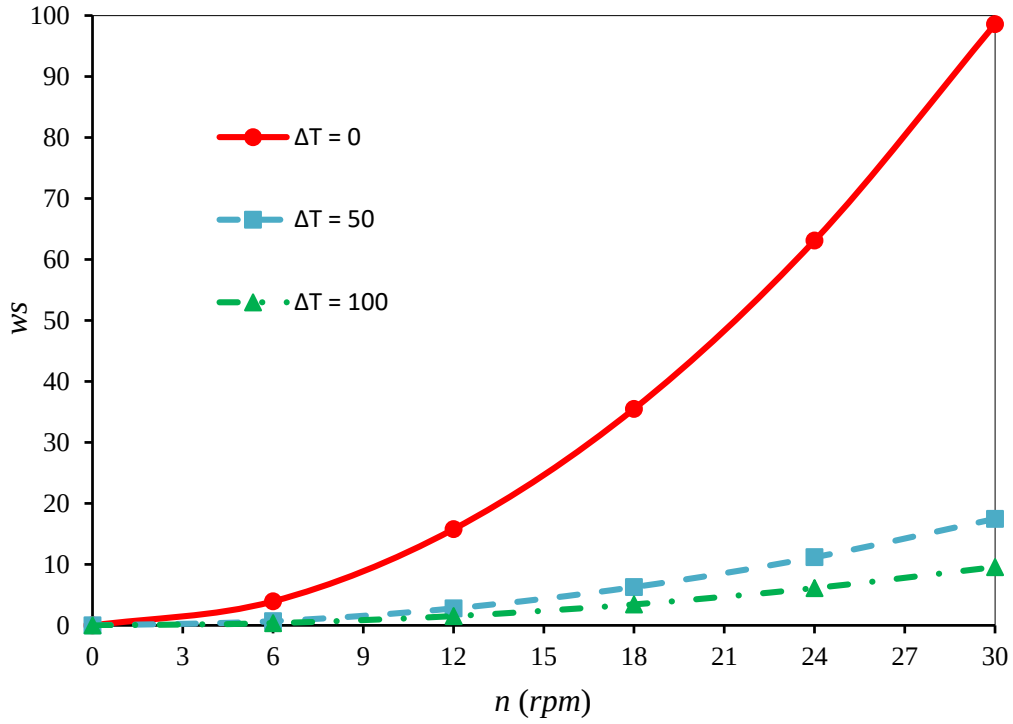

Fig. 15. Nondimensional deflection results versus the rotational speed changes for different amounts of temperature differences (ΔT)

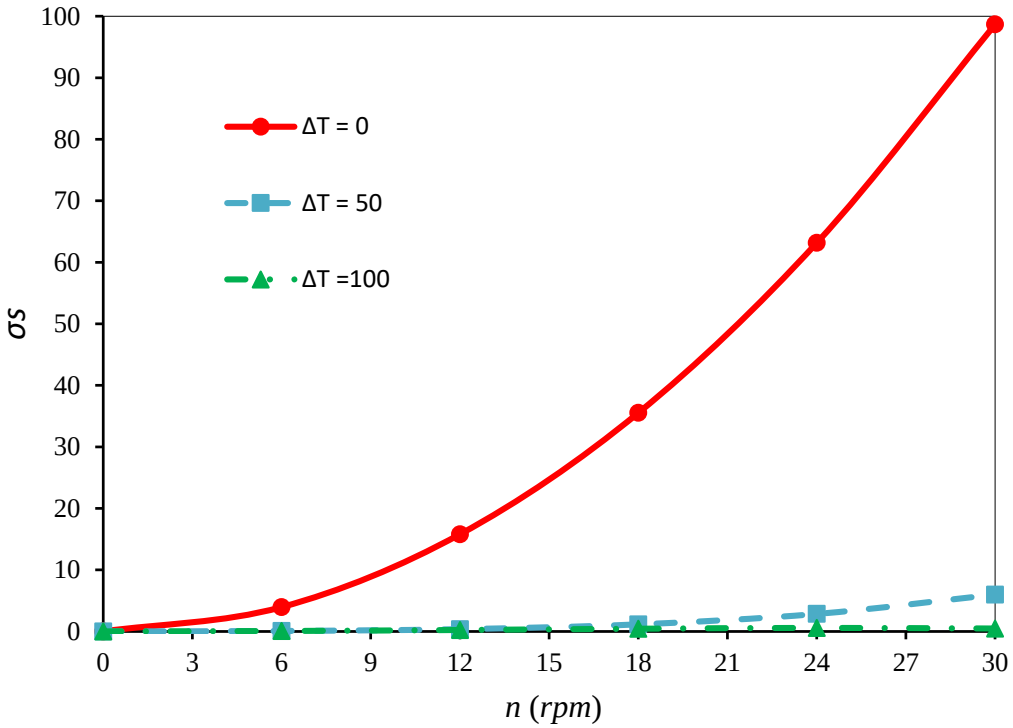

Fig. 16. Nondimensional von Mises stress results versus the rotational speed changes for different amounts of temperature differences (ΔT)

In this study, the effect of use of FGMs on the strength of the space structures has been studied in which the gravity force has been simulated by rotating the structure around its central axis. Recently, the use of FGMs has been tested for their effectiveness in other industries, in consequence, it has the potential to be used in the field of space exploration. Figs. 17 and 18 show the effects of the use of FGMs on deformation and stresses in the cylindrical space structure. Two graphs are plotted for different values of the g parameter to investigate the effect of material property changes. It is observed that with increasing the value of g, the intensity of changes is initially ascending, but gradually the slope of changes decreases, and increasing the value of g will not affect the results. By increasing the g parameter, the amount of deformation and stress in the structure decreases. For example, by increasing the g-parameter from zero to 5, the deformation of the structure decreases approximately threefold, which is about twice the reduction for von Mises stress. Therefore, it is concluded that the use of FGMs increases the strength of the structure, which is very desirable. As a result, thinner FGMs (which are also lighter) can be used for a space structure. Research on the use of FGMs in space structures can be considered by researchers in theory and practice. Another issue that is of particular importance for FGMs is their excellent performance against heat and high temperatures. This issue is very important in space structures and in order not to raise the temperature of space structures too much. Consequently, a heat shield is usually used to repel heat radiation from the sun or very high heat (in the shape of plasma) when the spacecraft enters the Earth's atmosphere (due to friction between the molecules of the atmosphere and the spacecraft body at very high speed). Therefore, the use of FGMs will not only increase the strength of the structure but also cause the repulsion of high temperatures in outer space.

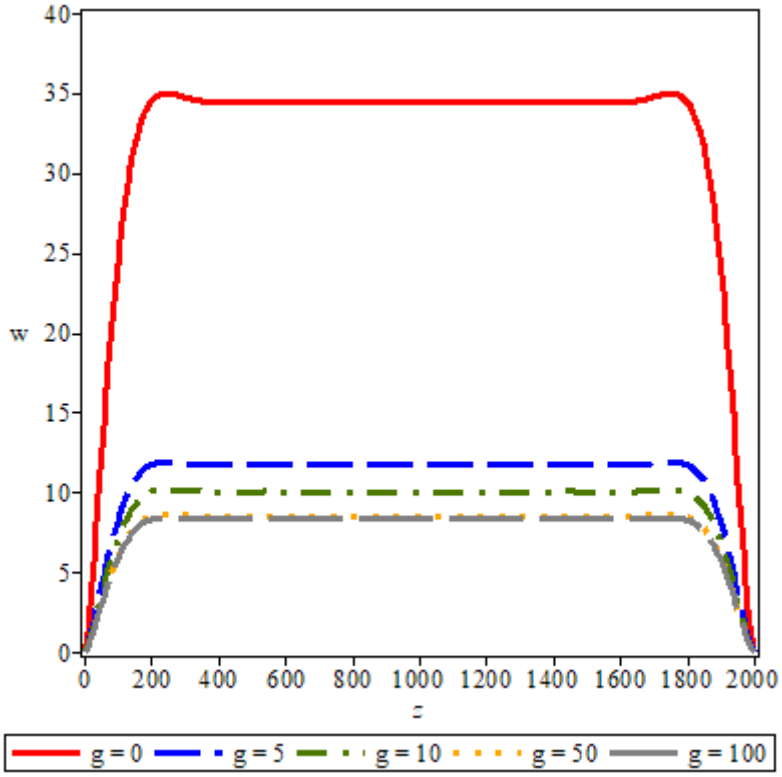

Fig. 17. Deformation results for different values of FGMs parameters (g)

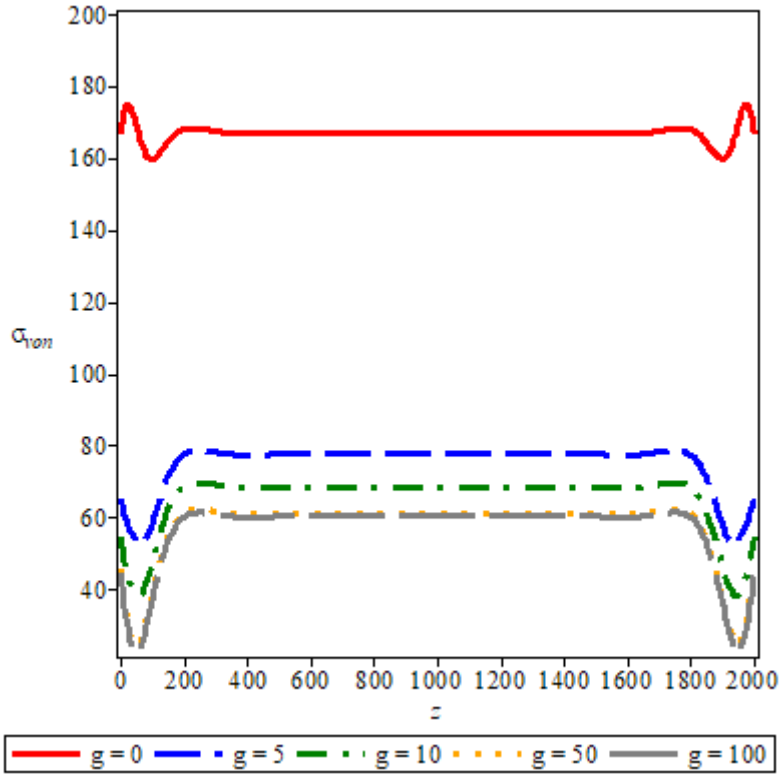

Fig. 18. von Mises stress results for different values of FGMs parameters (g)

As shown in Figs. 17 and 18, the use of FGM in the structure increases its resistance to applied mechanical loads. The results obtained for the deformation of the structure are now considered in Fig. 19 for increasing the g-parameter for conditions without temperature changes ($\Delta T = 0$) and considering temperature changes equal to $\Delta T = 50$℃. As can be expected, as the value of g increases, the deformation of the structure decreases and converges to a constant value (the result of which is also obtained in Figs. 17 and 18). It is observed that at the beginning of increasing the g parameter, the slope of the changes w is high and a very sharp drop can be observed. Therefore, selecting the value of g in the interval $0 < g < 5$ will cause the greatest changes in the mechanical response of the structure made of FGMs to the applied loads. A very important point according to Fig. 19 is the effect of thermal loads on the obtained results.

It is observed that in conditions where the temperature difference is equal to $\Delta T = 50$℃, the decrease in the amount of deformation w in the range of $0 < g < 5$ is much greater than in the case where the amount of temperature difference is zero ($\Delta T = 0$). In other words, the use of FGMs will expel most of the adverse effects of temperature changes. To better understand the above result, Fig. 20 is drawn with the same conditions as in Fig. 19, except that the vertical axis is not a deformation of the structure and is in fact a dimensionless deformation as w_f. The value of w_f indicates the ratio of changes in deflection for different values of the parameter g to the rise in the case where $g = 0$ (or in other words, the substance is isotropic and completely obeys the metal properties).

According to Fig. 20, it is observed that for $\Delta T = 50$℃, the use of FGMs will reduce the deformation in the structure by about 70%. The mentioned result for the case without temperature changes ($\Delta T = 0$) is only about 35% decrease. Therefore, the use of FGMs for the purpose of constructing space structures generally have beneficial results against the temperature effects.

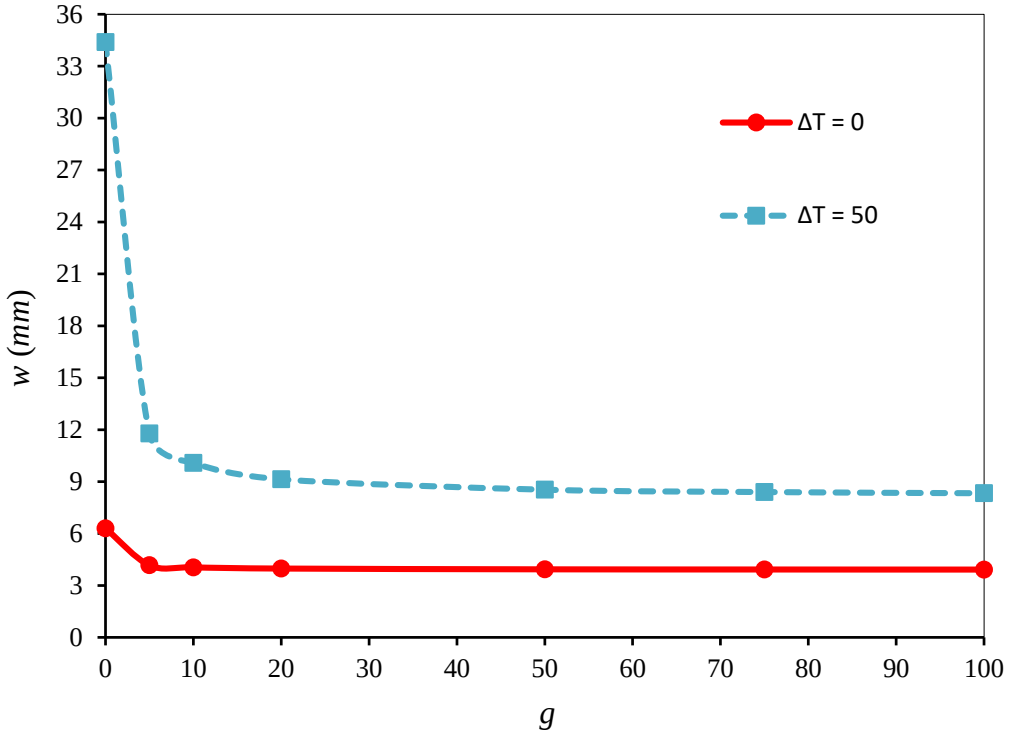

Fig. 19. Variations of deflection (w) versus parameter g in the FGM space structure for two types of temperature differences

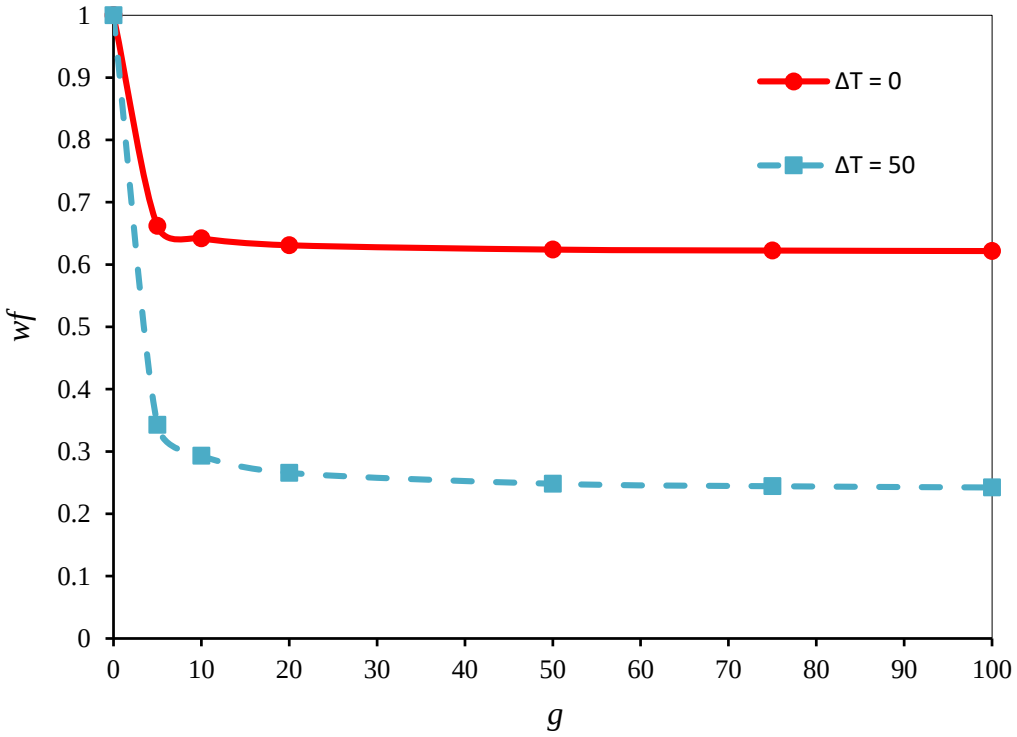

Fig. 20. Variations of dimensionless deflection (w_f) versus parameter g in the FGM space structure for two types of temperature differences

5.4. Different boundary conditions

In order to determine the behavior of different boundary conditions, Fig. 21 is plotted. In this three-dimensional presentation of results, one can see the nondimensional deflections for the vertical axis, dimensionless length for the longitudinal axis, and lateral axis is dedicated with the circumferential angle of the cylinder. To consider various boundary conditions, here clamped-clamped (C-C) and clamped-free (C-F) ones are investigated for the cylinder structure. First of all, as can be seen, deflections for all the circumferential nodes of the cylinder are obtained in the same values. Moreover, it is interesting to know that the maximum deflections are not related to the center of the length (for C-C) and one can observe two peaks in a symmetrical form. This is similar for both cases of boundaries. This may be because of the kind of loading. If we loaded the cylinder structure by a transverse line loading acted on the outer surface, the maximum deflections would be at the free edge (for C-F) and center of the length (for C-C). But as here the loading is applied as circumferential internal pressure, the case is different. Generally, this figure can present the fact that while the loading is an internal pressure acting in 360 degrees of the internal surface, the boundary conditions are less important.

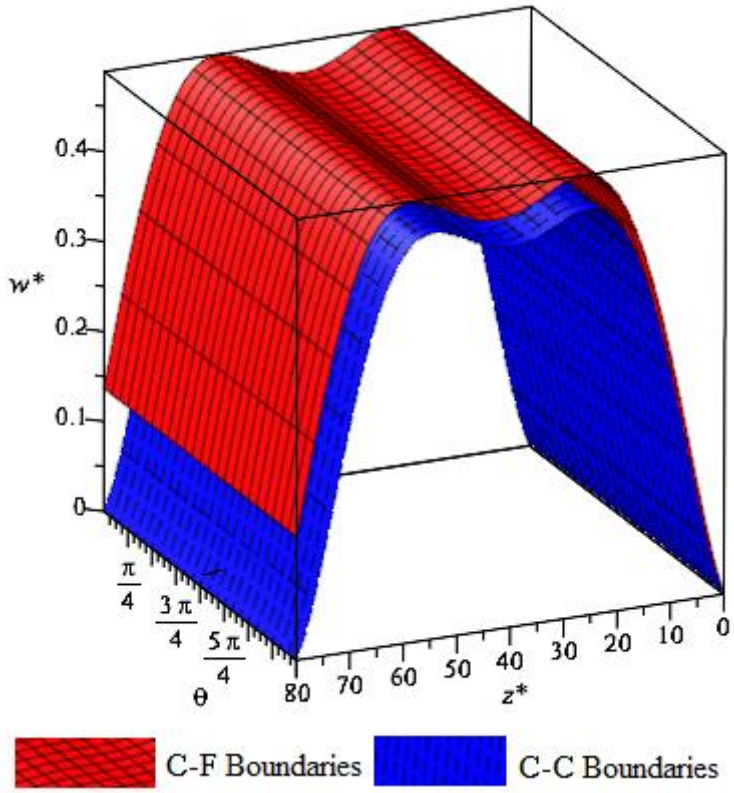

Fig. 21. Variations of dimensionless deflection versus dimensionless length and cylinder rotation angle in the FGM space structure for two types of boundary conditions

6. Conclusions and remarks

Mechanical simulation of cylindrical and torus-shaped structures with regard to normal living conditions in space has been discussed in this study (which should be given more attention in the future). The effect of artificial gravity acceleration on the mechanical strength of space structures, which are generally torus and cylindrical in terms of geometric shape, is a category that has been considered. In addition to the mechanical loads due to internal pressure, the temperature difference conditions inside and outside the structure (ΔT) are also considered in the analysis. The governing equations of the torus and cylindrical structures, which are intended to house individuals in outer space, have been derived based on the first-order shear deformation shell theory. The resulting governing equations (which are a set of partial differential equations) are then solved by the efficient SAPM solution method, and the

displacement field unknowns are obtained as functions of the problem variables. Some important results obtained from this study can be categorized as follows:

- Choosing the optimal and appropriate thickness of a rotating space structure that provides the required strength to maintain the integrity of the structure is the first important step for design. Deformation and stresses due to temperature differences (ΔT) strongly affect the results.
- The length of the cylindrical space structure (or R_d in torus structure), which rotates around its central axis, does not play an important role in determining the strength of the structure and only increases the internal capacity and, consequently, increases the cost of construction.
- The space structure according to its radius must rotate at a certain rotational speed to achieve the desired gravitational acceleration (equal to the gravitational acceleration on the Earth's surface) in the structure artificially. The greater the radius of rotation and the speed of rotation, the lower the strength of the structure to applied loads (mechanical and environmental loadings).
- Enhancement of the rotational speed increases the percentage of dimensionless deformation and stress w_s and σ_s created in the structure. However, the effect of this category on the results decreases with the development of the temperature difference (ΔT).
- The use of FG materials in space structures increases its strength against applied mechanical and especially thermal loads.

Acknowledgments: V.A. Eremeyev acknowledges the support of the Government of the Russian Federation (contract No.14.Y26.31.0031).

References

[1] J. Jaap Wijker, Mechanical Vibrations in Spacecraft Design, Springer-Verlag Berlin Heidelberg, 2004. DOI: 10.1007/978-3-662-08587-5

[2] A. Skullestad, O. Hallingstad, Vibration parameters identification in a spacecraft subjected to active vibration damping, Mechatronics, 8 (1998) 691-705.

[3] A. Calvi, P. Bastia, Mechanical architecture and loads definition for the design and testing of the Euclid spacecraft, Advances in aircraft and spacecraft science, 7 (2016) 225-242.

[4] L. K. Liu, G. T. Zheng, Parameter analysis of PAF for whole-spacecraft vibration isolation, Aerospace Science and Technology, 11 (2007) 464-472.

[5] S. Strauss, Space medicine at the NASA-JSC, neutral buoyancy laboratory, Aviat Space Environ Med, 79 (2008) 732-3.

[6] B. Yang, W. Yuan, Y. Shang, J. Wang, B. Wei, Numerical and experimental study of a novel three-fluid membrane dehumidification method applied to spacecraft humidity control, Journal of Membrane Science, 530 (2017) 112-124.

[7] J. F. Parmer, D. L. Buskirk, The thermal radiation characteristics of spacecraft temperature control louvers in the solar space environment, Editor(s): Gerhard B. Heller, Thermophysics of Spacecraft and Planetary Bodies, Academic Press, (1967) 695-708.

[8] R. X. Meyer, Chapter 7 - Spacecraft thermal design, Editor(s): Rudolf X. Meyer, Elements of Space Technology, Academic Press, (1999) 269-305.

[9] Y. Cao, D. Cao, G. He, L. Liu, Thermal alternation induced vibration analysis of spacecraft with lateral solar arrays in orbit, Applied Mathematical Modelling, 86 (2020) 166-184.

[10] E. A. Thornton, Y. A. Kim, Thermally induced bending vibrations of a flexible rolled-up solar array, Journal of Spacecraft & Rockets, 30 (1993) 438-448.

[11] D. W. Gulick, E. A. Thornton, Thermally-induced vibrations of a spinning spacecraft boom, Acta Astronautica, 36 (1995) 163-176.

[12] J. Li, S. Yan, R. Cai, Thermal analysis of composite solar array subjected to space heat flux, Aerospace Science and Technology, 27 (2013) 84-94.

[13] Z. Shen, H. Li, X. Liu, G. Hu, Thermal-structural dynamic analysis of a satellite antenna with the cable-network and hoop-truss supports, Journal of Thermal Stresses, 42 (2019) 1339-1356.

[14] Z. Shen, G. Hu, Thermally induced vibrations of solar panel and their coupling with satellite, International Journal of Applied Mechanics, 5 (2013) 1350031.

[15] L. J. Fan, Z. H. Xiang, Suppressing the Thermally Induced Vibration of Large-Scale Space Structures via Structural Optimization, Journal of Thermal Stresses, 38 (2015) 1-21.

[16] J. Zhang, Z. Xiang, Y. Liu, Quasi-Static Shape Control of Flexible Space Structures by Using Heaters, AIAA Journal, 51 (2013) 1003-1007.

[17] Z. Shen, G. Hu, Thermoelastic–Structural Analysis of Space Thin-Walled Beam Under Solar Flux, AIAA Journal, 57 (2019) 1781-1785.

[18] Sh. Dastjerdi, B. Akgöz, Ö. Civalek, On the effect of viscoelasticity on behavior of gyroscopes, International Journal of Engineering Science, 149 (2020) 103236.

[19] Sh. Dastjerdi, B. Akgöz, On the statics of fullerene structures, International Journal of Engineering Science, 142 (2019) 125-144.

[20] Sh. Dastjerdi, B. Akgöz, Ö. Civalek, M. Malikan, V. A. Eremeyev, On the non-linear dynamics of torus-shaped and cylindrical shell structures, International Journal of Engineering Science, 156 (2020) Article no 103371.

[21] Sh. Dastjerdi, B. Akgöz, New static and dynamic analyses of macro and nano FGM plates using exact three-dimensional elasticity in thermal environment, Composite Structures, 192 (2018) 626-641.

[22] M. Malikan, V. A. Eremeyev, A new hyperbolic-polynomial higher-order elasticity theory for mechanics of thick FGM beams with imperfection in the material composition, Composite Structures, 249 (2020) 112486.

[23] B. Karami, M. Janghorban, On the mechanics of functionally graded nanoshells, International Journal of Engineering Science, 153 (2020) 103309.

[24] A. M. Dehrouyeh-Semnani, E. Dehdashti, M. R. Hairi Yazdi, M. Nikkhah-Bahrami, Nonlinear thermo-resonant behavior of fluid-conveying FG pipes, International Journal of Engineering Science, 144 (2019) 103141.

[25] M. H. Jalaei, Ö. Civalek, On dynamic instability of magnetically embedded viscoelastic porous FG nanobeam, International Journal of Engineering Science, 143 (2019) 14-32.

[26] Sh. Dastjerdi, M. Malikan, R. Dimitri, F. Tornabene, Nonlocal elasticity analysis of moderately thick porous functionally graded plates in a hygro-thermal environment, Composite Structures, (2020) 112925. https://doi.org/10.1016/j.compstruct.2020.112925

[27] Sh. Dastjerdi, Y. Tadi Beni, M. Malikan, A comprehensive study on nonlinear hygro-thermo-mechanical analysis of thick functionally graded porous rotating disk based on two quasi-three-dimensional theories, Mechanics Based Design of Structures and Machines, An International Journal, (2020). https://doi.org/10.1080/15397734.2020.1814812

[28] B. Karami, M. Janghorban, A. Tounsi, Nonlocal strain gradient 3D elasticity theory for anisotropic spherical nanoparticles, Steel and Composite Structures, 27 (2018) 201-216.

[29] B. Karami, M. Janghorban, L. Li, On guided wave propagation in fully clamped porous functionally graded nanoplates, Acta Astronautica, 143 (2018) 380-390.

[30] B. Karami, M. Janghorban, A. Tounsi, Variational approach for wave dispersion in anisotropic doubly-curved nanoshells based on a new nonlocal strain gradient higher order shell theory, Thin-Walled Structures, 129 (2018) 251-264.

[31] B. Akgöz, Ö. Civalek, Buckling analysis of functionally graded microbeams based on the strain gradient theory, Acta Mechanica, 224 (2013) 2185-2201.

[32] B. Akgöz, Ö. Civalek, Free vibration analysis of axially functionally graded tapered Bernoulli–Euler microbeams based on the modified couple stress theory, Composite Structures 98 (2013) 314-322.

[33] B. Karami, M. Janghorban, A. Tounsi, Novel study on functionally graded anisotropic doubly curved nanoshells, European Physical Journal Plus, 135 (2020). https://doi.org/10.1140/epjp/s13360-019-00079-y

[34] M. Malikan, F. Tornabene, R. Dimitri, Nonlocal three-dimensional theory of elasticity for buckling behavior of functionally graded porous nanoplates using volume integrals, Materials Research Express, 5 (2018) 095006.

[35] B. Karami, M. Janghorban, T. Rabczuk, Forced Vibration Analysis of Functionally Graded Anisotropic Nanoplates Resting on Winkler/Pasternak-Foundation, Computers, Materials & Continua, 62 (2020) 607-629.

[36] H. Zharfi, Creep relaxation in FGM rotating disc with nonlinear axisymmetric distribution of heterogeneity, Theoretical and Applied Mechanics Letters, 9 (2019) 382-390.

[37] G. L. She, H. B. Liu, B. Karami, On resonance behavior of porous FG curved nanobeams, Steel and Composite Structures, 36 (2020) 179-186.

[38] E. Barchiesi, M. Spagnuolo, L. Placidi, Mechanical metamaterials: a state of the art, Mathematics and Mechanics of Solids, 24 (2019) 212-234.

[39] F. dell'Isola, P. Seppecher, J. Jacques Alibert et al., Pantographic metamaterials: an example of mathematically driven design and of its technological challenges, Continuum Mechanics and Thermodynamics, 31 (2019) 851-884.

[40] M. Malikan, N. S. Uglov, V. A. Eremeyev, On instabilities and post-buckling of piezomagnetic and flexomagnetic nanostructures, International Journal of Engineering Science, 157 (2020) Article no. 103395.

[41] V. A. Eremeyev, J.-F. Ganghoffer, V. Konopinska-Zmyslowska, N. S. Uglov, Flexoelectricity and apparent piezoelectricity of a pantographic micro-bar, International Journal of Engineering Science, 149 (2020) 103213.

[42] V. A. Eremeyev, G. Rosi, S. Naili, Transverse surface waves on a cylindrical surface with coating, International Journal of Engineering Science, 147 (2020) 103188.

[43] A. Eyvazian, D. Shahsavari, B. Karami, On the dynamic of graphene reinforced nanocomposite cylindrical shells subjected to a moving harmonic load, International Journal of Engineering Science, 154 (2020) 103339.

[44] B. Karami, D. Shahsavari, M. Janghorban, On the dynamics of porous doubly-curved nanoshells, International Journal of Engineering Science, 143 (2019) 39-55.

[45] M. Malikan, M. Krasheninnikov, V. A. Eremeyev, Torsional stability capacity of a nano-composite shell based on a nonlocal strain gradient shell model under a three-dimensional magnetic field, International Journal of Engineering Science, 148 (2020) 103210.

[46] J. Chróscielewski, F. dell'Isola, V. A. Eremeyev, A. Sabik, On rotational instability within the nonlinear six-parameter shell theory, International Journal of Solids and Structures, 196–197 (2020) 179-189.

[47] S. Brischetto, A general exact elastic shell solution for bending analysis of functionally graded structures, Composite Structures, 175 (2017) 70-85.